The Astrophysical Journal, 981:26 (31pp), 2025 March 1 https://doi.org/10.3847/1538-4357/adaea7
© 2025. The Author(s). Published by the American Astronomical Society.
OPEN ACCESS

Evolution of X-Ray Gas in SN 1987A from 2007 to 2021: Ring Fading and Ejecta Brightening Unveiled through Differential Emission Measure Analysis

Lei Sun[1,2,3], Salvatore Orlando[4], Emanuele Greco[3,4,5], Marco Miceli[4,5], Yang Chen[1,2], Jacco Vink[3], and Ping Zhou[1,2]

[1] Department of Astronomy, Nanjing University, Nanjing 210023, People's Republic of China; l.Sun@nju.edu.cn
[2] Key Laboratory of Modern Astronomy and Astrophysics, Nanjing University, Ministry of Education, People's Republic of China
[3] Anton Pannekoek Institute & GRAPPA, University of Amsterdam, P.O. Box 94249, 1090 GE Amsterdam, The Netherlands
[4] INAF-Osservatorio Astronomico di Palermo, Piazza del Parlamento 1, 90134 Palermo, Italy
[5] Università degli Studi di Palermo, Dipartimento di Fisica e Chimica E. Segrè, Piazza del Parlamento 1, 90134 Palermo, Italy
Received 2024 August 14; revised 2025 January 13; accepted 2025 January 23; published 2025 February 24

Abstract

As the nearest supernova (SN) observed since Kepler's SN of 1604, SN 1987A provides an unprecedented opportunity to study in detail the early evolution of supernova remnants. Despite extensive studies through both observations and simulations, there is still an urgent need for a more effective approach to integrate the results from two sides. In this study, we conducted a detailed differential emission measure (DEM) analysis on the XMM-Newton observations taken in 2007 to 2021 to characterize the continuous temperature structure of SN 1987A, which can be better compared with simulations. The X-ray plasma exhibits a temperature distribution with a major peak at ∼0.5–1 keV and a high-temperature tail extending to $\gtrsim$5 keV. The emission measure (EM) of the major peak started to decline around 2014, while the EM of the tail continued increasing and appears to have formed a secondary peak at ∼3–5 keV in recent years. Our DEM results are consistent with simulations, which help to further identify the major peak as originating from the equatorial ring and the secondary peak as arising from the newly shocked ejecta. Together with the simulations, our DEM analysis reveals recent fading of the ring and brightening of the ejecta in X-rays from SN 1987A. Additionally, we observed a recent decrease in the centroid energy of the Fe K line, providing further evidence of newly shocked ejecta.

Unified Astronomy Thesaurus concepts: X-ray astronomy (1810); Supernova remnants (1667); Interstellar medium (847)

1. Introduction

The supernova remnant (SNR) is the leftover of a supernova (SN) explosion, formed by the interaction of the SN ejecta with the ambient circumstellar material (CSM) and interstellar medium (ISM). Therefore, it provides a crucial perspective to study the physical and chemical properties of both the ejecta and the CSM/ISM. These studies can help us gain a better understanding of SNR-related physics, such as remnant evolution and its metal/energy feedback, collisionless shock physics, cosmic-ray acceleration mechanism, etc. Additionally, they allow us to trace back the progenitor properties and explosion mechanisms of SNe.

SN 1987A was a Type II SN exploded in the Large Magellanic Cloud (LMC), whose progenitor is a blue supergiant (BSG; R. M. West et al. 1987), and was first detected on 1987 February 23. As the nearest SN observed since Kepler's SN of 1604, SN 1987A provides an unprecedented opportunity to study in detail the SN–SNR connection and the early phase of SNR evolution. The remnant of SN 1987A is represented by its well-known triple-ring CSM system, where one equatorial ring (ER) together with two outer rings constitutes an hourglass-like structure. Starting from ∼4000 days after the explosion, several "hot spots" emerged in the optical band as a result of the SN blast wave (i.e., the forward shock) encountering the dense inner layer of ER (e.g., G. Sonneborn et al. 1998; S. S. Lawrence et al. 2000). Soon after, the main body of the ER began to be impacted and heated by the forward shock, leading to a dramatic increase in its soft X-ray brightness at ∼6000 days (e.g., S. Park et al. 2005). From then on, the blast wave continuously interacted with the ER, making it shine across all the energy bands. Until recently, the forward shock seems to have traversed the main ER but still propagates into the high-latitude materials, indicated by the decreasing optical, infrared, and soft X-ray fluxes, and the still increasing hard X-ray flux (e.g., C. Fransson et al. 2015; R. G. Arendt et al. 2016; J. Larsson et al. 2019; L. Sun et al. 2021; A. P. Ravi et al. 2024). On the other hand, the evidence of a pulsar wind nebula (PWN; or a cooling neutron star) at the center of SN 1987A has recently been found based on the NuSTAR detection of its hard-band nonthermal emission (E. Greco et al. 2022) and the JWST detection of emission lines due to its ionizing radiation (C. Fransson et al. 2024).

SN 1987A is also one of the few SNRs that have been studied in great detail through three-dimensional (3D) hydrodynamic and magnetohydrodynamic (MHD) simulations tracing their long-term evolution from the explosion all the way to the remnant phase (e.g., S. Orlando et al. 2015, 2019, 2020; M. Ono et al. 2020). The simulations have successfully reproduced the multiwavelength emission of SN 1987A, where the synthetic images, light curves, and spectra are well comparable with the observations up to now. In particular, the synthetic high-resolution X-ray spectra show an impressive consistency with the Chandra HETG (M. Miceli et al. 2019) and XMM-Newton RGS (E. Greco et al. 2022) observations at multiple epochs.

Original content from this work may be used under the terms of the Creative Commons Attribution 4.0 licence. Any further distribution of this work must maintain attribution to the author(s) and the title of the work, journal citation and DOI.

Despite extensive study of SN 1987A through both observations and simulations, several unresolved issues persist. Specifically, there is still a need for a more effective approach to connect observations with simulations. Most previous studies on SN 1987A adopted discrete-temperature (either two-temperatures or three-temperatures) plasma models to fit its X-ray spectra (e.g., S. Park et al. 2004, 2006; F. Haberl et al. 2006; S. A. Zhekov et al. 2006, 2009, 2010; K. Heng et al. 2008; R. Sturm et al. 2010; D. Dewey et al. 2012; K. A. Frank et al. 2016; E. Bray et al. 2020; D. Alp et al. 2021; E. Greco et al. 2021, 2022; A. P. Ravi et al. 2021, 2024; L. Sun et al. 2021; C. Maitra et al. 2022). As summarized by D. Alp et al. (2021, see Table 6 therein), these works found plasma temperatures in the range of ∼0.5–4 keV, with a low-temperature component at ∼0.5 keV, a high-temperature component at ∼2–4 keV, and, for some of them, a third intermediate-temperature component at ∼1 keV. However, while these discrete-temperature models can approximately fit the spectra and characterize the average properties of the plasma, they may be inadequate to fully represent the complex structure of SN 1987A and are difficult to directly compare with the continuous parameter distributions evaluated from simulations. More importantly, interpretations based on this modeling might also be biased.

This study aims to characterize the continuous temperature structure of the X-ray gas in SN 1987A through a detailed differential emission measure (DEM) analysis of the long-term XMM-Newton observations. The results of the DEM analysis will be compared with MHD simulation predictions, which will in turn provide a more comprehensive interpretation of the observations and enhance our understanding of remnant evolution. Similar attempts have been made by S. A. Zhekov et al. (2006, 2009) using Chandra LETG/HETG data and by D. Alp et al. (2021) using reflection grating spectrometer (RGS) + NuSTAR data. However, their results are not consistent with each other, and neither of them agree well with the simulations, which motivated us to perform further investigations into this issue.

We describe the observations and the data reduction procedures in Section 2, describe the DEM model and present the DEM analysis results in Section 3, discuss the DEM results in Section 4 by comparing observations with simulations, and make our conclusions in Section 5.

2. Observations and Data Reduction

SN 1987A has been regularly monitored in X-rays. In this work, we utilized a set of XMM-Newton observations taken since 2007, which is similar to those used in L. Sun et al. (2021), but with two additional epochs: the first was taken in 2020 November (PI: F. Haberl), and the second was obtained in 2021 December (PI: L. Sun), representing the most recent XMM-Newton observation of the evolution of SN 1987A. For each observation, we used both the RGS and the EPIC-pn exposures. The high energy resolution of RGS can help to detect and resolve the numerous emission lines in 0.35–2.5 keV, which is crucial for our spectral modeling. EPIC-pn has a large effective area and a complete energy coverage up to 10 keV, providing further constraints on the continuum and the high-temperature plasmas. The details of all observations are summarized in Table 1.

All the data were processed using the XMM-Newton Science Analysis Software (SAS, version 18.0.0)[6] with the latest calibration files. We extracted the RGS and the EPIC-pn spectra following the procedures described in L. Sun et al. (2021). The spectra were then optimally rebinned adopting the J. S. Kaastra & J. A. M. Bleeker (2016) optimal binning scheme.

3. DEM Analysis

In this section, we describe the DEM model, verify the validity and the reliability of the model, and then present the DEM analysis results of SN 1987A. We used XSPEC (version 12.12.1)[7] with AtomDB 3.0.9[8] for spectral analysis, and adopted C statistic. Unless otherwise specified, in this paper, the metal abundances are with respect to their solar values (J. Wilms et al. 2000), and the error bars represent the 1σ uncertainties.

3.1. DEM Model

Our DEM model is similar to those used in S. A. Zhekov et al. (2006, 2009) and D. Alp et al. (2021), which is basically an extended version of the XSPEC model `c6pvmkl` (J. R. Lemen et al. 1989; K. P. Singh et al. 1996) that works not only on the collisional-ionization-equilibrium plasmas but also on the nonequilibrium-ionization (NEI) plasmas.

The volume emission measure (EM) of a thermally emitting plasma, defined as $\mathrm{EM} \equiv \int n_e n_{\mathrm{H}} dV$, can be described by a function of temperature as

$$\mathrm{EM} = \int d(\mathrm{EM}) = \int \phi(T) dT = \int T\phi(T) d(\ln T), \quad (1)$$

where $\phi(T)$ is called the DEM function, representing the temperature distribution of the plasma. In our model, the DEM function $\phi(T)$ is parameterized by an Mth-order Chebyshev series as

$$\phi(T) = \alpha e^{\omega(T)}, \ \omega(T) = \sum_{k=1}^{M} a_k P_k(T), \quad (2)$$

where α is the normalization parameter, a_k is the coefficients, P_k is the Chebyshev polynomial of order k, and M is the maximum order of the Chebyshev series. T denotes the (quasi-) continuous electron temperature, which is represented by N temperature bins (T_i, $i = 1, 2, \ldots, N$) logarithmically spaced in 0.1–10 keV. For each T_i, the X-ray spectrum is calculated by a single `vnei` model, with $T_e = T_i$ and the EM given by $\phi(T_i)$. In order to lower the number of free parameters and to keep the model as simple as possible, we assume that the ionization parameter $\tau_i = (n_e t)_i$, where t denotes the elapsed time since the gas was shocked, is a power-law function of the temperature following S. A. Zhekov et al. (2006, 2009) and D. Alp et al. (2021), i.e.,

$$\tau_i = \tau_{1\,\mathrm{keV}} \left(\frac{T_i}{1\ \mathrm{keV}} \right)^{\beta}, \quad (3)$$

[6] https://www.cosmos.esa.int/web/xmm-newton/sas
[7] https://heasarc.gsfc.nasa.gov/xanadu/xspec/
[8] http://www.atomdb.org/

Table 1
Observations

ObsID[c]	Date	Age (days)	t_{exp}[a] (ks)		∑GTI[b] (ks)	
			EPIC-pn	RGS	EPIC-pn	RGS
0406840301	2007 Jan 17	7267	106.9	111.3	61.1	109.8
0506220101	2008 Jan 11	7627	110.1	114.3	70.7	102.4
0556350101	2009 Jan 30	8012	100.0	101.9	66.4	101.8
0601200101	2009 Dec 11	8327	89.9	91.8	82.4	91.7
0650420101	2010 Dec 12	8693	64.0	65.9	52.7	65.9
0671080101	2011 Dec 2	9048	80.6	82.5	64.2	80.6
0690510101	2012 Dec 11	9423	68.0	69.9	59.4	69.8
0743790101	2014 Nov 29	10,141	78.0	79.6	56.4	79.4
0763620101	2015 Nov 15	10,492	64.0	65.9	58.0	65.8
0783250201	2016 Nov 2	10,845	72.4	74.3	50.3	74.2
0804980201	2017 Oct 15	11,192	77.5	79.4	27.8	79.3
0831810101	2019 Nov 27	11,964	32.4	34.9	11.1	34.8
0862920201	2020 Nov 24	12,328	77.6	79.7	57.8	72.8
0884210101	2021 Dec 28	12,727	90.6	89.4	75.2	86.1

Notes.
[a] Total exposure times.
[b] Total good time intervals after background flare removal.
[c] Observation ID.

where $\tau_{1\,\mathrm{keV}}$ is the ionization parameter at 1 keV, and β is the power-law index. Despite the fact that the X-ray-emitting plasma may have a nonuniform complex chemical composition, we assume that its metal abundances are identical across all temperature bins. This assumption is viable, given that the majority of the X-ray emission originates from the shocked CSM and from the shocked outermost layers of ejecta (expected with abundances similar to those of CSM), and thus, only small variations of abundances are expected from the different plasma components. Following R. Sturm et al. (2010) and the references therein, with abundances converted to those in J. Wilms et al. (2000), the abundances of N, O, Ne, Mg, Si, S, and Fe are set as free parameters, while those of He (set to 2.57), C (0.14), Ar (0.76), Ca (0.49), and Ni(0.98) are fixed. Then, the final spectrum is the sum of all the spectra in all the temperature bins (therefore, the DEM model could also be regarded as a combination of N `vnei` components).

The maximum order of the Chebyshev series M and the total temperature bin number N may affect the modeling performance and the fitting results, therefore should be chosen with caution based on the data fitted. A rather large M and N can help to achieve a high-temperature resolution and to capture delicate structures in DEM distribution, but will introduce more free parameters, consume a lot of computer time, and may lead to overfitting when applied to low-quality data. On the other hand, a rather small M and N may be not enough to reproduce the DEM distribution and lose information in the data. We have tried different combinations of M and N in our test cases (see Appendix A for details), and finally fix them as $M = 7$ and $N = 40$, which achieves the best performance for our RGS + EPIC-pn spectral fitting of SN 1987A. Following the naming logic of `c6pvmkl` model, we call this DEM model `c7pvnei` hereafter.

Apart from the DEM component, the overall setup of the spectral model is similar to those in L. Sun et al. (2021). The X-ray emission from SN 1987A is subjected to absorption from both the Galactic and the LMC ISM, which are characterized by two `tbvarabs` components. The Galactic absorption is fixed at $N_{\mathrm{H,Gal}} = 6 \times 10^{20}\,\mathrm{cm}^{-2}$ with solar abundances, while the LMC absorption $N_{\mathrm{H,LMC}}$ is set as a free parameter (see the discussions below) with the average LMC abundances given by S. C. Russell & M. A. Dopita (1992). A `gsmooth` component and a `vashift` component are involved to account for the line broadening effect and the Doppler shift, respectively, and their parameters are fixed to the best-fit values given in L. Sun et al. (2021; see the values in Table 2 therein).

The LMC absorption $N_{\mathrm{H,LMC}}$ is not tied between different observations due to two major reasons. First, from a physical perspective, while it is improbable that there would be varying large-scale ISM absorption, there remains the possibility of an evolving local absorption component arising from both the unshocked CSM and the unshocked ejecta of SN 1987A. As pointed out by L. Sun et al. (2021), a density of $1 \times 10^4\,\mathrm{H\,cm}^{-3}$ and a path length of 0.01 pc will result in a measurable local absorption $N_{\mathrm{H}} \sim 0.3 \times 10^{21}\,\mathrm{cm}^{-2}$. This local absorption may change over time due to the expansion of the ejecta, potential destruction of CSM clumps, and rapid changes in the X-ray surface brightness distribution of the remnant itself (see the Chandra images in K. A. Frank et al. 2016). Second, from a technical standpoint, it is nearly impossible to simultaneously fit all 14 observations with $N_{\mathrm{H,LMC}}$ tied up, since it will introduce too many free parameters and consume significant computational resources. By setting N_{H} as a free parameter, we obtained a column density varying between $\sim$2.2 and $2.8 \times 10^{21}\,\mathrm{cm}^{-2}$, with a mean value $\sim 2.5 \times 10^{21}\,\mathrm{cm}^{-2}$, which is consistent with the local absorption scenario. In the time interval we have studied, the absorption column density was found to be increasing in general with some fluctuations. One possible explanation could be that as the ejecta expand, more and more unshocked ejecta material will be projected onto the ER region, and thus increase the total absorption column density. But on the other hand, the

Table 2
Parameters of the Test Models

	kT_e (keV)	$n_e t$ (10^{11} s cm^{-3})
1-T vnei	0.8	1.0
2-T vnei	0.5	10.0
	2.5	1.0
3-T vnei	0.3	10.0
	1.0	3.4
	4.0	1.0

expansion of the ejecta will result in a decrease in its density; thereby, we may expect to see a decrease in the absorption column density at some point in the future. A further discussion on the local absorption will be interesting but may be beyond the scope of this paper.

As a brief summary, our spectral model can be described as $\texttt{tbvarabs}_{\rm Gal} \times \texttt{tbvarabs}_{\rm LMC} \times$ gsmooth × vashift × c7pvnei. There are 18 free parameters in total: the LMC absorption column density ($N_{\rm H,LMC}$), 7 Chebyshev polynomial coefficients (a_k, $k = 1, 2, \ldots, 7$), 7 metal abundances (N, O, Ne, Mg, Si, S, and Fe), the ionization parameter at 1 keV ($\tau_{1\ \rm keV}$), the ionization parameter index (β), and finally the normalization (α). As a comparison, a three-temperature model (3-T vnei or 3-T vpshock) with a similar parameter setup (e.g., D. Alp et al. 2021; E. Greco et al. 2022) will have ∼17 free parameters. Thereby, the DEM model, with only one more free parameter than the traditional discrete-temperature models, is able to characterize the (quasi-)continuous distribution of the hot plasma among a wide range in temperature space, which provides us a unique insight into the real thermal condition of the gas and the underlying physics. In view of the large free parameter number and the potential degeneracy between different parameters, we ran a Markov Chain Monte Carlo (MCMC) simulation using the XSPEC chain command after every fit, in order to determine the 1σ errors. The MCMC simulation was running using the Goodman–Weare algorithm with 40 walkers and a total length of 10^5.

3.2. Test on Simulated Data

Before applying the DEM model to the real RGS + EPIC-pn data, it is necessary to test the validity and the reliability of the model. At least, we need to ensure that if the X-ray gas in SN 1987A indeed has a bimodal or trimodal temperature distribution as previous studies suggested (e.g., S. A. Zhekov et al. 2006, 2009; D. Alp et al. 2021), the DEM model should be able to reproduce those features.

Therefore, we constructed three test models that consist of one, two, and three vnei components, respectively. The electron temperatures and the ionization parameters of the vnei components in each test model are listed in Table 2. The EMs of the vnei components were set to the values that give a similar flux as SN 1987A (∼7.8×10^{-12} erg cm^{-2} s^{-1} in 0.5–2 keV band at its peak level around 2013, see, e.g., L. Sun et al. 2021). Other parameters, such as the absorption column density and metal abundances, were set following the average values obtained in L. Sun et al. (2021). We then simulated the 80 ks RGS (including the first- and second-order spectra of RGS1 and RGS2) and EPIC-pn spectra based on the three test models using the XSPEC fakeit command. The simulated spectra were then optimally rebinned adopting the J. S. Kaastra & J. A. M. Bleeker (2016) optimal binning scheme, just like the real data. Finally, we fit the DEM model to these simulated spectra (we fit the 0.35–2.5 keV RGS and the 0.3–10 keV EPIC-pn spectra simultaneously). Figures 1(a)–(c) show the fitting results. We found the DEM model can reproduce the one-, two-, and three-temperature components very well, as shown by the single, double, and triple peaks seen in the fitting results. However, we noticed that the fitted peaks can be slightly shifted from the "true values." For example, in Figure 1(c), the 4 keV peak is shifted to ∼5 keV, and the 1 keV peak is also shifted a little bit to higher temperature. A possible explanation for this could be that the 0.3 and 1 keV peaks are not perfectly separated by the DEM fitting, and thus, the low-temperature EM may be slightly overestimated, which pushes the 1 and 4 keV peaks a little bit to higher temperatures. The degeneracy between temperature and ionization parameters may contribute as well. This level of systematic uncertainty will not alter the conclusions of this work.

The above test models are still quite simple and idealized, while the real X-ray gas in SN 1987A could have a much more complicated temperature structure. In order to examine the performance of the DEM model in a more complex situation, we adopted the synthetic 80 ks RGS (the first order spectrum of RGS1) and EPIC-pn spectra of SN 1987A at its age of 27 in 2014 from E. Greco et al. (2022) as another test. The spectra were synthesized based on the B18.3 model in S. Orlando et al. (2020) and M. Ono et al. (2020), which has been well constrained by multiwavelength observations of the progenitor star, the SN explosion, and the SNR. The synthetic spectra represent a wide temperature distribution ranging from ∼0.2–5 keV, as shown by the red line in Figure 1(d). The DEM fitting basically reproduces the temperature distribution with a main peak at ∼0.6 keV and a high-temperature tail extending to ∼4 keV. Some fine structures in the original distribution have been smoothed out due to the DEM model resolution limit. There is a fake structure seen at very low (0.1–0.2 keV) temperature. Similar features can also be seen in some cases when we apply the DEM model to the real SN 1987A data (see Section 3.3 for details). Given the large uncertainties of the DEM at low temperatures, we consider them as most likely the fake features caused by the low signal-to-noise ratio of the spectra at the very low energy band. We note that, given their rather low temperatures, these (fake) features make little contribution to the total X-ray emission, and thus will not alter the DEM profile at higher temperatures and the conclusions of this work.

With the tests above, we demonstrate the capability of the DEM model to capture the complex temperature structure of SN 1987A. Whether the X-ray gas is concentrated in two or three major components, or has a more continuous distribution, the DEM model is able to reproduce these features with good accuracy and reliability.

3.3. Application to Real Data

We applied our DEM model to each observation listed in Table 1, by fitting the 0.35–2.5 keV RGS and the 0.3–10 keV EPIC-pn spectra simultaneously. The obtained temperature distribution of the X-ray gas and its temporal evolution in 2007–2021 is shown in Figure 2. The examples of the fitted spectra are shown in Figure 3. We leave the detailed best-fit parameters, their 1σ uncertainties, the MCMC corner plots, and

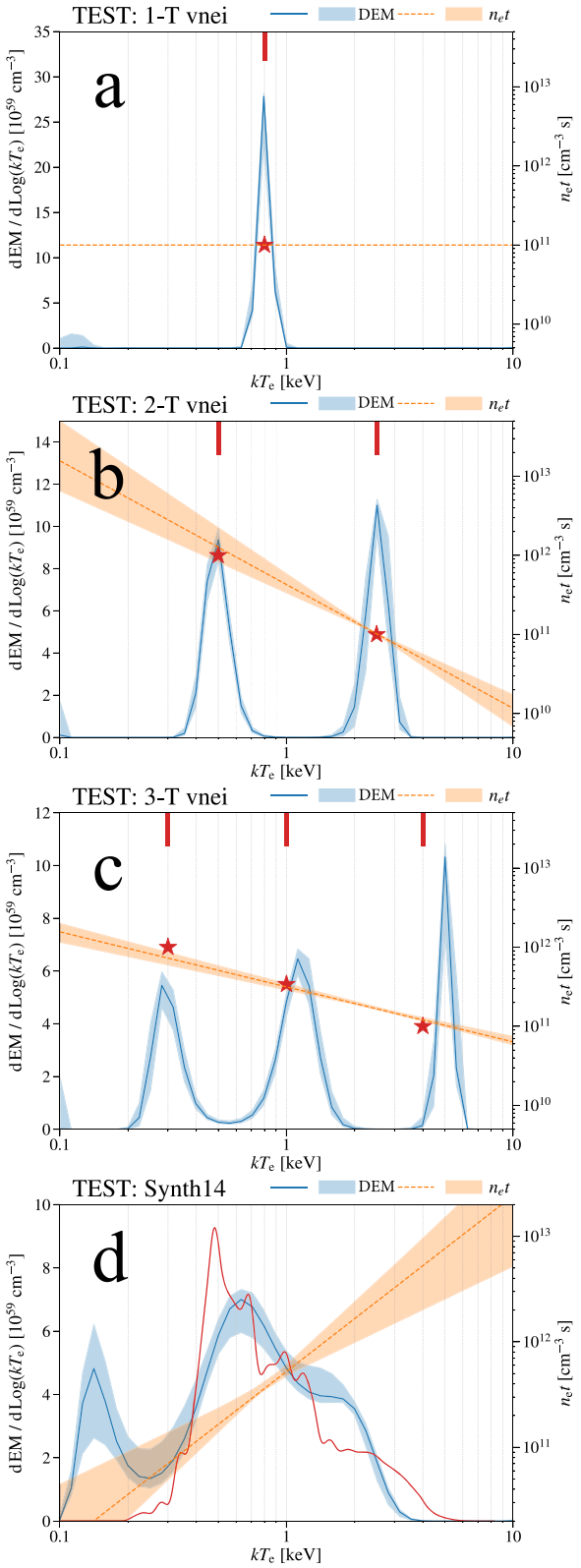

Figure 1. The DEM model applied on simulated spectra. Panels (a)–(c) show the DEM fitting results of the 1-T, 2-T, and 3-T `vnei` spectra, respectively. The red lines and stars denote the temperatures and ionization parameters used for simulating the spectra, the blue lines and areas show the best-fit DEM distributions and their 1σ uncertainties, and the orange dashed lines and areas show the best-fit $n_e t$ distributions and their 1σ uncertainties. Panel (d) shows the fitting results of the synthetic spectra representing the simulated X-ray emission of SN 1987A in 2014 (E. Greco et al. 2022). The red line denotes the synthetic DEM distribution.

the fitted spectra from all the epochs in Appendix B. The DEM model provides a significantly better fit to the data than the discrete-temperature models. The C statistics range from 1796 to 2246 with degrees of freedom (dof) ranging from 1584 to 1766. With only one additional parameter (thereby $\Delta\mathrm{dof} = -1$), the DEM model achieves an average improvement of the C statistic of $\overline{\Delta C} \sim -38$ (ranging from -4 to -109) compared with a 3-T `vnei` model. However, we note that, despite significant improvements, the DEM modeling is still far from perfect and leaves some residuals in the fitted spectra. One of the notable residual features is observed at the O lines, which may be due to other mechanisms such as charge exchange, resonant scattering, and absorption of the foreground hot gas. We leave the discussions on O lines in a companion paper (Sun et al. 2025).

We found the X-ray gas in SN 1987A generally follows a similar temperature distribution during the ∼15 yr. Rather than concentrating on two or three well-separated peaks, it centers on only one major peak at ∼0.5–1 keV in most of the epochs, while there is always a tail extending to the high-temperature end (up to $\gtrsim$5 keV).

In order to better identify the major peak and the high-temperature tail, and estimate their mean temperatures and total EMs, we fitted the obtained DEM distributions with two Gaussian profiles. We found that, for all the epochs, the double-Gaussian profile was capable of fitting the DEM distribution, and thus, two temperature components (namely, the major peak and the high-temperature tail) were identified. The average temperature of the two components, as well as the EM ratio between them ($\mathrm{EM_{highT}}/\mathrm{EM_{major}}$), is shown in the bottom right panel of Figure 2. The average temperature of the major peak increased from ∼0.5 to ∼1 keV over a decade. The high-temperature tail has an average temperature ∼2–5 keV, while no significant variation patterns can be observed. The total EM of the major peak kept climbing in the first few years, reached its maximum at around 2011–2014, and then started to decline. This is consistent with previous results on the soft band (e.g., 0.5–2 keV) light curves (e.g., K. A. Frank et al. 2016; D. Alp et al. 2021; L. Sun et al. 2021; A. P. Ravi et al. 2024) and the low-temperature plasma component EMs (e.g., D. Alp et al. 2021; A. P. Ravi et al. 2021; L. Sun et al. 2021). On the other hand, the high-temperature tail kept existing and increasing in its EM during the whole period. As a result, the EM ratio between the high-temperature tail and the major peak has been continuously increasing, from ∼0.1 at around 2007 to $\gtrsim$0.2 after 2014, and reaching ∼0.4 at around 2020 (the bottom right panel in Figure 2). This suggests a greater contribution of the high-temperature plasma to the X-ray emission in recent years. As a consequence, the high-temperature tail becomes more and more significant in the DEM profile, and appears to have formed a secondary peak in 2020–2021.

In the DEM distribution of some observations (e.g., 2008, 2011, and 2017), we found a potential peak at very low temperature ($\lesssim$0.2 keV) with large uncertainties. As we have discussed in Section 3.2, these are most likely the fake features caused by the low signal-to-noise ratio of the spectra at the very low energy band. However, it is still possible that these features are from a real plasma component with a rather low temperature and high density (therefore a low shock velocity to achieve a low postshock temperature). We note that such a component has been observed at the early stage of the X-ray remnant of SN 1987A, when the SN shock just encountered

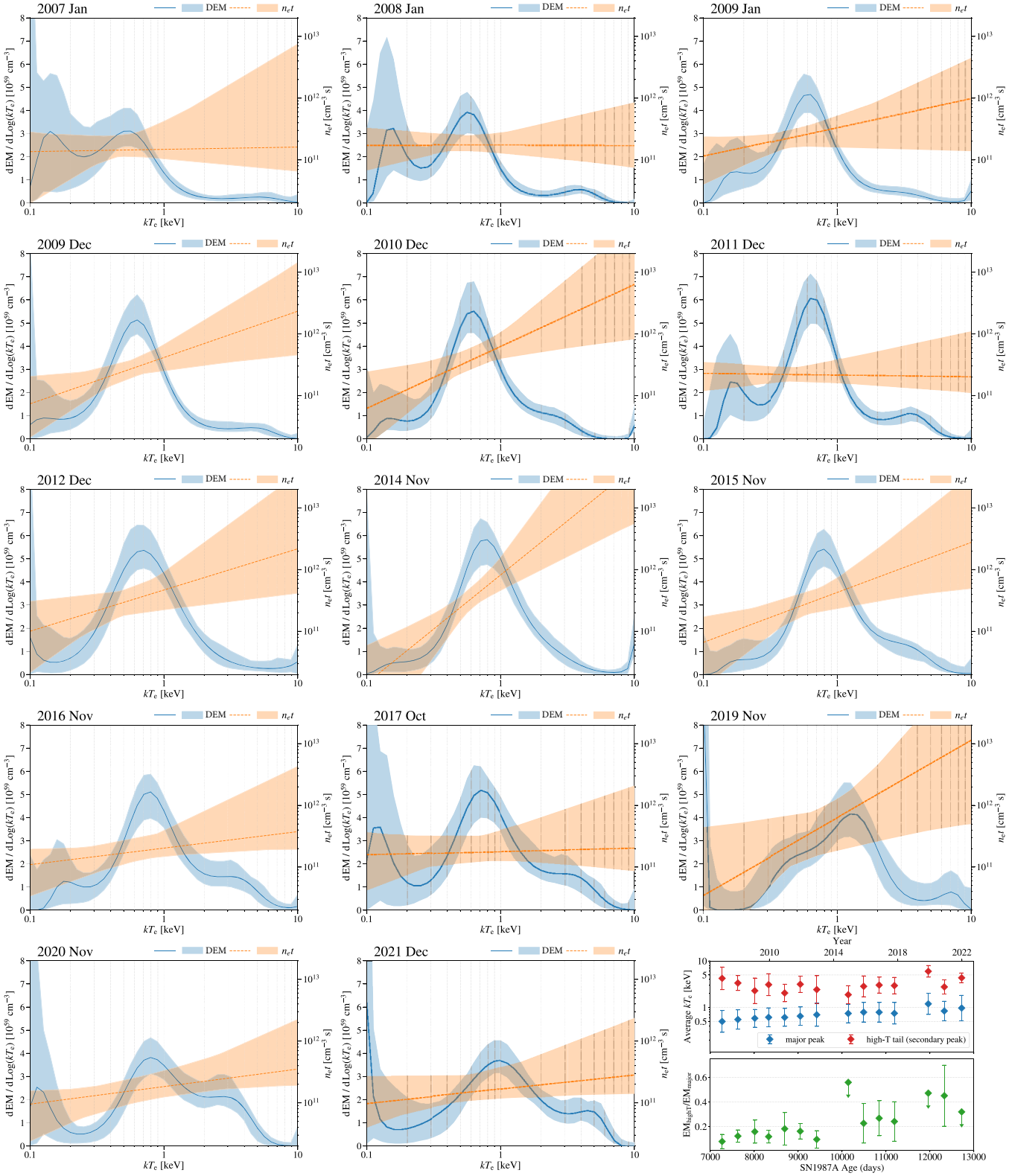

Figure 2. DEM fitting results for SN 1987A in different epochs based on XMM-Newton RGS and EPIC-pn observations. In the bottom right panel, we present the average temperatures of the major peak and the high-temperature tail (the blue and red data points in the upper subpanel, respectively), and the ratio between the EMs of the two components (the green data points in the lower subpanel).

with the dense inner part of the ER. For example, S. Park et al. (2004) reported a plasma component with $kT_e \sim 0.22$ keV and $n_e \sim 7500\,\mathrm{cm}^{-3}$ resulting from the slow transmitted shock into the dense inner ring. Another possible interpretation of this low-temperature component could be the shocked stellar wind from the BSG progenitor of SN 1987A. The typical temperature of such a kind of shocked stellar wind is ~0.1 keV (e.g., J. Castor et al. 1975). At last, the emission

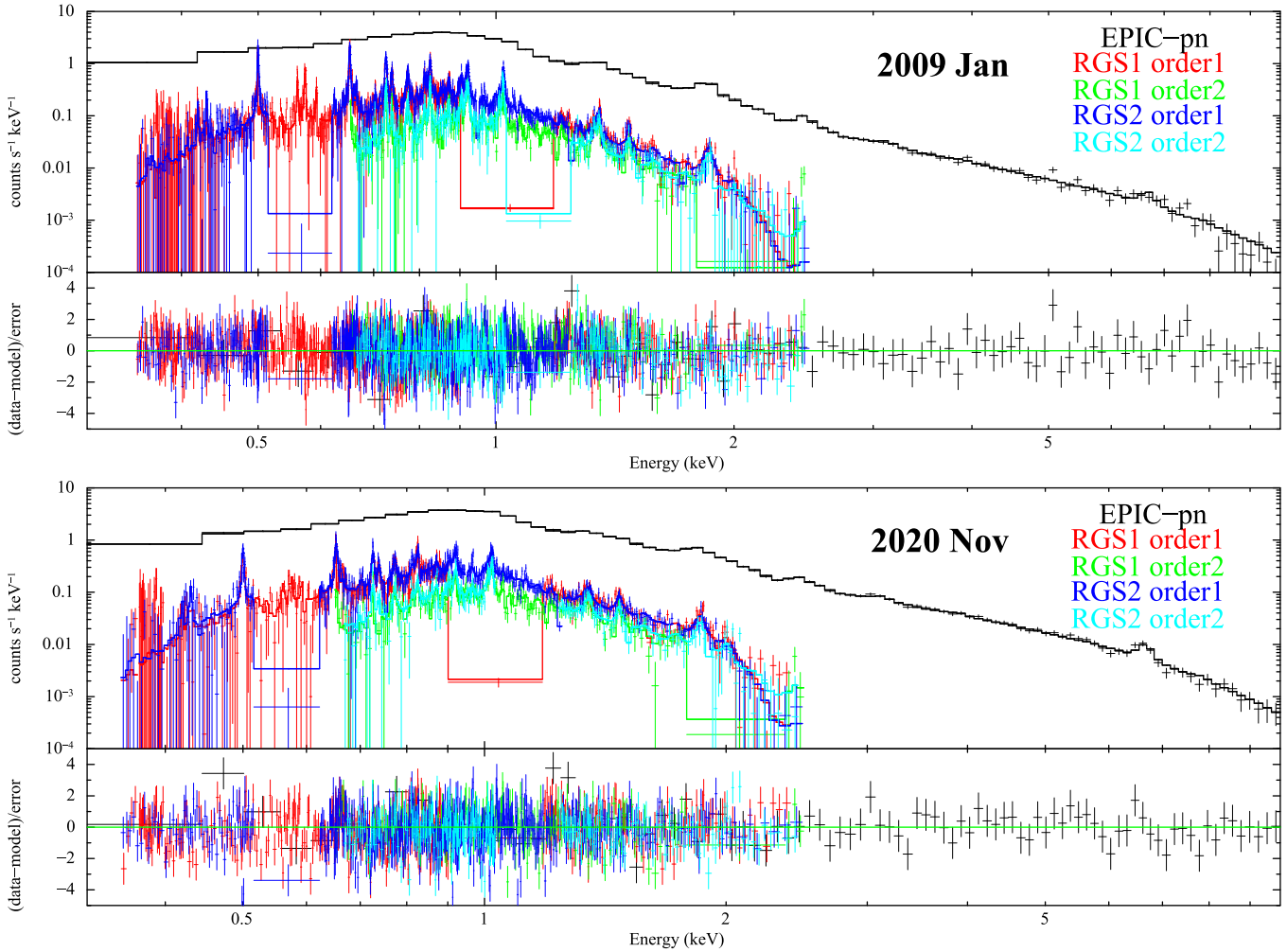

Figure 3. Two examples of the fitted RGS + EPIC-pn spectra with residuals, taken from 2009 January and 2020 November. The spectra from other epochs are presented in Appendix B.

from the local hot bubble, if it has not been fully subtracted during the background subtraction process, may also contribute to this low-temperature component. Nevertheless, the fact that this low-temperature feature comes and goes with time is still against the interpretation as a real shock component.

4. Discussions

4.1. Comparison with MHD Simulations: Interpretation of the DEM Results

SN 1987A is one of the few SNRs for which people have performed comprehensive 3D MHD simulations tracing their long-term evolution from the onset of the SN all the way to the remnant phase (e.g., S. Orlando et al. 2020). It provides us with an unprecedented opportunity to connect simulations with observations—not only in the sense that the long-term, multiwavelength observations of SN 1987A (including its progenitor star, the SN explosion, and its remnant) set detailed constraints on the initial conditions and help to regulate the simulations but also in the sense that the simulation results, together with the synthesized observables (including the multiwavelength images, light curves, and spectra), are well comparable with observations, which may in turn help us to better understand the observations and make predictions.

One of the most impressive outcomes of the SN 1987A simulations is that it shows how well the synthesized X-ray spectra match with the actual observations. E. Greco et al. (2022) synthesized the SN 1987A X-ray spectra in three epochs (2012, 2014, and 2020) based on the B18.3 model in S. Orlando et al. (2020) and M. Ono et al. (2020), and compared them with XMM-Newton RGS, XMM-Newton EPIC-pn, Chandra ACIS-S, and NuSTAR FPMA observations. Without performing any fit, they found the synthesized thermal spectra reproduce the observed <10 keV spectra very well at all epochs for all instruments (see Figure 2 in E. Greco et al. 2022). The simulations provide a continuous distribution of the plasma in a large parameter space, which was adopted in X-ray spectra synthesis. The first row of Figure 4 shows the simulated plasma EM distributions of SN 1987A in the kT_e–n_et diagram at different epochs. Spectral fitting results from previous studies adopting two-temperature (L. Sun et al. 2021) and three-temperature (E. Greco et al. 2022) models are also plotted in order to compare with simulations. We found that, even though the 2-T and 3-T models may represent some kinds of average properties of the plasma, they are still too simplified to describe the complex structure of the remnant.

Our DEM modeling results provide a unique perspective to compare observations with simulations. The second and third rows of Figure 4 present the DEM distributions of the X-ray

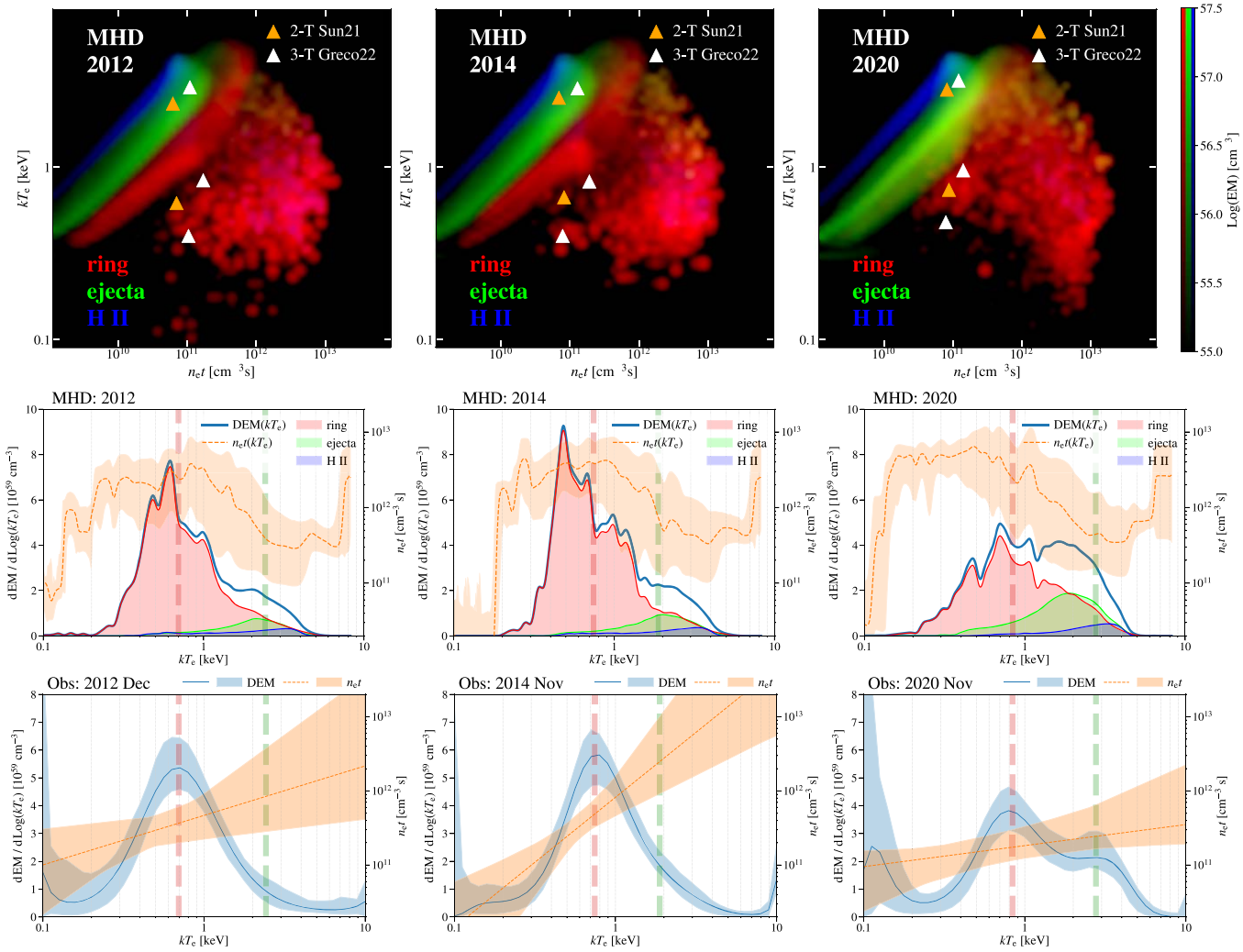

Figure 4. Comparison between MHD simulations and the DEM fitting results of SN 1987A. Top: simulated plasma EM distributions in kT_e–n_et diagrams (based on the B18.3 model in S. Orlando et al. 2020), overlaid with 2-T (L. Sun et al. 2021) and 3-T (E. Greco et al. 2022) spectral fitting results. Different components (i.e., ring, ejecta, and H II region) are indicated by different colors (i.e., red, green, and blue). Middle: simulated DEM distributions (blue solid lines) and EM-weighted n_et distributions (orange dashed lines). Bottom: DEM fitting results, same as those in Figure 2. The red and green dashed lines in the middle and bottom panels denote the average temperatures of the major peak and the high-temperature tail (the secondary peak) obtained from the observations, respectively.

gas in SN 1987A obtained from simulations and observations, respectively. In 2012 and 2014, simulations indicate that the majority of EM concentrates at ∼0.6 keV, which is dominated by the ER and forms a major peak in the DEM curve. The shocked H II region and ejecta materials have higher temperatures (up to ∼5 keV), which result in a tail in the DEM distribution to the high-temperature ends. In 2020, simulations predict a decrease in the EM of the ER-dominated low-temperature plasmas, resulting in a weakening of the major peak. On the other hand, the amount of the shock-heated ejecta materials has been significantly increasing, which raises the high-temperature tail and makes it comparable with the major peak. The DEM fitting results agree well with the simulations in almost all respects: the temperature and the EM of the major peak, the existence of a high-temperature tail, and the overall evolution of the DEM profile. This consistency not only strengthens the reliability of both sides but also helps us to get a better understanding of SN 1987A. In particular, as described above, we found a dramatic decline of the major peak and a rapid rising of the tail (the emergence of a secondary high-temperature peak) in the recent few years based on DEM analysis. Together with simulation results, this reveals the fading of the ER and the brightening of the shocked ejecta.

Despite the general consistency in most aspects, there are still some discrepancies between the MHD simulations and the observations, such as the average temperatures of the major peak and the high-temperature tail (the secondary peak), the absolute value of the DEM, and the n_et distributions. The observed average temperatures of the major and secondary peak appear to be slightly higher than those in simulations, which may suggest a higher shock velocity. The absolute DEM derived from our modeling is slightly lower than the simulation expectations. This may indicate an overall lower density of the shocked gas. However, we note that the simplified DEM model may smooth out the fine structures, leading to lower average values. Additionally, the difference in metal abundances may also lead to different DEM values. Our DEM modeling suggests a flat or positive correlation between n_et and kT_e (i.e., $\beta \gtrsim 0$) for most of the observations. The EM-weighted n_et according to simulations exhibits an increase with kT_e at very low temperatures ($\lesssim$0.3 keV), a plateau around ∼0.3–1 keV, then a decrease in ∼1–5 keV, and finally an increase again at

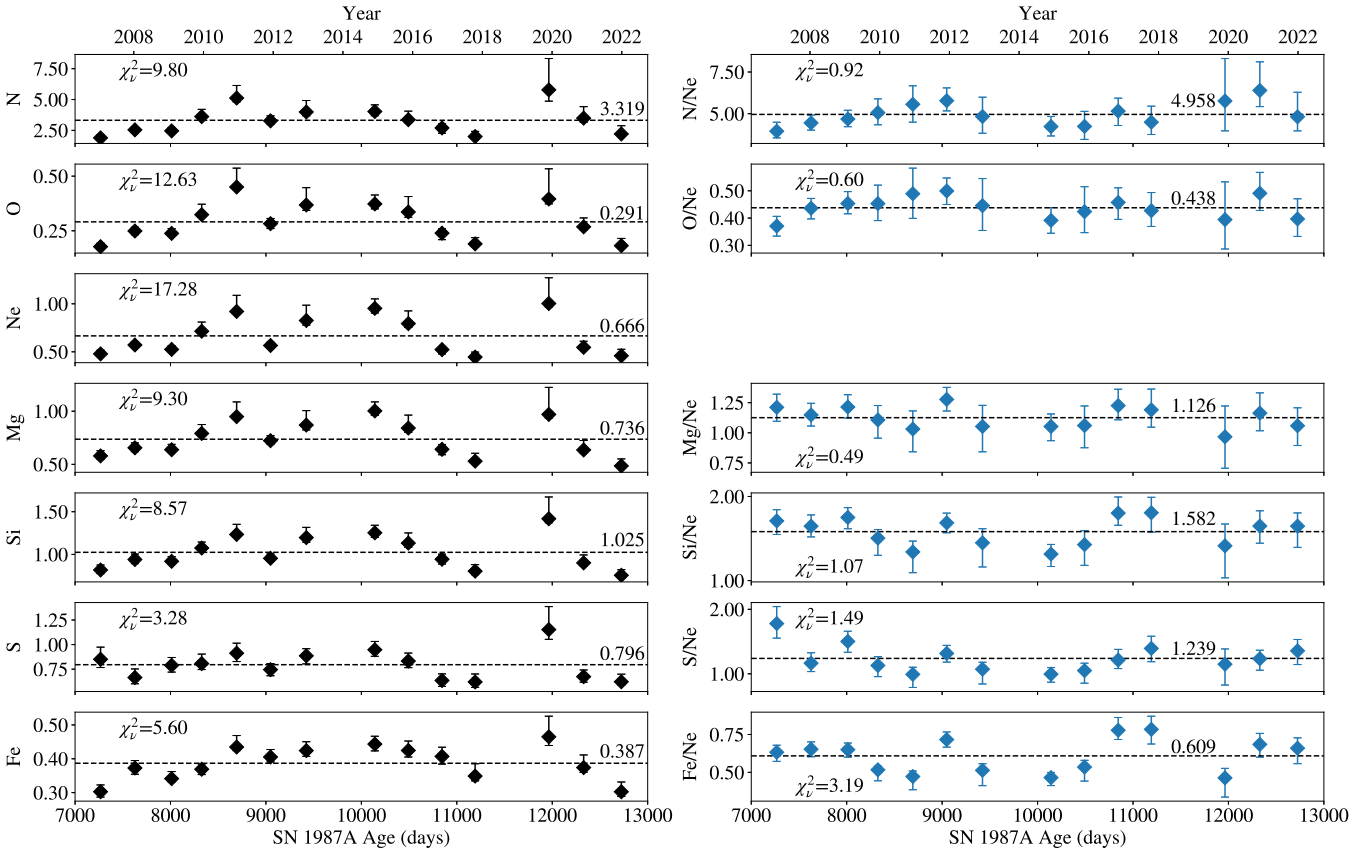

Figure 5. Metal abundances (left) and abundance ratios with respect to Ne (right) in SN 1987A. The black dashed lines indicate the mean values. Reduced chi-squares $\chi^2_\nu = \chi^2/\mathrm{dof}$ are calculated based on the mean values. For a p-value of 0.002 ($\sim 3\sigma$ level), the critical reduced chi-square is $\chi^2_{\nu,\mathrm{c}} \approx 2.50$ for 13 degrees of freedom.

very high temperatures ($\gtrsim$5 keV). However, the uncertainty of the fitted $n_\mathrm{e}t$ and the scattering of the simulated $n_\mathrm{e}t$ are both large. We leave a detailed discussion on the $n_\mathrm{e}t$–kT_e correlation in Section 4.3.

Recently, C. Maitra et al. (2022) performed an in-depth analysis on the XMM-Newton EPIC-pn observations of SN 1987A, by simultaneously fitting the spectra from all epochs with a three-temperature plasma model. They considered different metal abundances between different components and found that the abundances of the "hot" component are significantly higher than those of the "warm" and "cooler" components, for which they suggested the "hot" component originated from the reverse shock-heated ejecta. Figure 5 shows the metal abundances obtained from our DEM analysis. In our DEM model, the abundances are assumed to be identical at different temperatures, in order to limit the number of free parameters and to keep the model as simple as possible. Therefore, the abundances we obtained should be taken as the (EM-weighted) average values in SN 1987A. Even though the MHD simulations and the DEM distributions both indicate a recently brightened ejecta component, we did not find an increase in the average metal abundances. On the contrary, after a plateau around 2009–2016 ($\sim$8000–11,000 days), the abundances have been gradually decreasing and recently got back to the level they were around 2007 ($\sim$7000 days). This is consistent with the findings by L. Sun et al. (2021) based on 2-T fitting, and indicates that the ER has higher metal abundances (or say a lower hydrogen context) compared with the ambient H II region, and is now fading out. Although the shocked ejecta becomes increasingly dominant in X-ray emission, the decreasing average metal abundances suggest that the reverse shock has not yet reached the inner metal-rich core. This is also supported by simulations and optical observations, which show the outermost layer of the ejecta is dominated by hydrogen-rich materials (e.g., C. Fransson et al. 2013; J. Larsson et al. 2016; M. Ono et al. 2020; S. Orlando et al. 2020). However, the most recent JWST NIRSpec observations indicate that the inner Fe-rich ejecta are now starting to interact with the reverse shock (J. Larsson et al. 2023). Therefore, we are expecting to see the corresponding X-ray emission in the near future.

The metal abundances we obtained with DEM modeling are systematically higher than those obtained by L. Sun et al. (2021) and E. Greco et al. (2022) based on 2-T and 3-T fittings. Furthermore, we note that the 3-T models tend to give slightly higher abundances than 2-T models. This phenomenon has been noticed for a long time in X-ray spectroscopic studies, especially in those associated with the spectral fitting for ellipticals, groups, and clusters of galaxies, which is referred as "Fe bias" or "Si bias" (e.g., D. A. Buote 2000). It is found that, for a plasma that has an intrinsic wide continuous temperature distribution, an oversimplified 1-T modeling of the spectrum may result in underestimated metal abundances. Introducing more temperature components will improve the fit and provide unbiased constraints on abundances. The underlying mechanism could be that the 1-T models (or any discrete-temperature models) may overestimate the continuum emission, since part of the "continuum" is actually the

pseudocontinuum formed by numerous faint emission lines from other (unconsidered) temperature components. Similar phenomena have also been noticed and discussed in the context of pure-metal plasma by E. Greco et al. (2020), where they suggested a high-resolution spectroscopic study, especially on the resolved radiative recombination continuum emission, may help to disentangle the degeneracy between metal abundances and EM. In this sense, our results provide an up-to-date most unbiased constraint on the average metal abundances of SN 1987A.

4.2. Comparison with Previous Studies: Improvements and Advantages

Most of the previous studies on SN 1987A adopted discrete-temperature (either two-temperature or three-temperature) plasma models to fit its X-ray spectra (e.g., S. Park et al. 2004, 2006; F. Haberl et al. 2006; S. A. Zhekov et al. 2006, 2009, 2010; K. Heng et al. 2008; R. Sturm et al. 2010; D. Dewey et al. 2012; K. A. Frank et al. 2016; E. Bray et al. 2020; D. Alp et al. 2021; E. Greco et al. 2021, 2022; A. P. Ravi et al. 2021, 2024; L. Sun et al. 2021; C. Maitra et al. 2022). As summarized by D. Alp et al. (2021, see Table 6 therein), these works found plasma temperatures mostly in the range of ∼0.5–4 keV, with a low-temperature component ∼0.5 keV, a high-temperature component ∼2–4 keV, and, for some of them, an intermediate component ∼1 keV. As mentioned in Section 4.1, even though these discrete-temperature models may in some way characterize the average properties of the plasma, they are still oversimplified, and we are still looking for a better approach to describe the complex structure of the remnant and to compare with simulations.

For now, only a few attempts have been made to model the continuous temperature distribution of SN 1987A. S. A. Zhekov et al. (2006, 2009) made the first try by applying a "distribution of shocks (DS)" model (which is very similar to our DEM model described in Section 3.1, but is based on `vpshock` rather than `vnei`) to Chandra LETG/HETG data taken in 2004 and 2007. They found a bimodal temperature distribution that peaks at ∼0.5 and ∼2.2–3 keV. Recently, D. Alp et al. (2021) performed a similar analysis on RGS + NuSTAR data taken in 2012 to 2020. However, their results suggested three peaks in the continuous temperature distribution, at ∼0.3, ∼0.9, and ∼4 keV, respectively (the separation between the 0.3 and 0.9 keV peaks is marginally significant). The results from the above studies are not consistent with each other (which could be due to the observations they used being from different epochs and instruments), and neither of them agrees well with the simulations.

Our results are different from those of S. A. Zhekov et al. (2006, 2009) and D. Alp et al. (2021), while some similarities can be found. Rather than well-separated two or three peaks, we found only one major peak in most of the observations. The major peak is quite wide, overlapping with the 0.5 keV peak in S. A. Zhekov et al. (2006, 2009) and the 0.3 and 0.9 keV peaks in D. Alp et al. (2021). The high-temperature peak is not very significant in our results until 2020, which appears as a tail extending to ∼5 keV in most of the observations. For a detailed comparison with previous studies, we summarize the major improvements and advantages of our work below:

1. *Data*. S. A. Zhekov et al. (2006, 2009) adopted Chandra LETG/HETG observations of 2004 and 2007. Limited by the relatively low effective area and the low luminosity of SN 1987A at that time, the spectra may have lower statistics compared with those taken by XMM-Newton RGS and EPIC-pn after 2007. In particular, they may have fewer constraints on the hard-band continuum, and thus the high-temperature plasma components. D. Alp et al. (2021) jointly fitted both the RGS and NuSTAR spectra, which provide a much wider energy coverage and result in good constraints on both the low- and high-temperature gas. However, since the spectra in different energy bands are from different observations taken by different instruments, their results may be subjected to systematic uncertainties arising from, e.g., temporal variation of SN 1987A between RGS and NuSTAR observations taken in different epochs,[9] cross-calibration uncertainties between RGS and NuSTAR, and the energy gap between RGS and NuSTAR spectra (at ∼2–3 keV, which leads to a missing of the S lines and the underlying continuum). We note that some of these systematic uncertainties have been investigated in Appendix D of D. Alp et al. (2021). They simultaneously fitted the RGS + EPIC-pn + NuSTAR data from several epochs with their continuous-temperature model, and introduced a variable cross-normalization constant for each instrument in order to account for cross-calibration uncertainties. They found that including the EPIC-pn data does not qualitatively affect their conclusions, although there could be a hint that the two low-temperature peaks are less distinct (see the upper left panel of their Figure D2 in D. Alp et al. 2021). In this work, we jointly fitted the RGS + EPIC-pn spectra, which are taken at the same time for each observation and cover a wide energy range from 0.35 to 10 keV without any gap. Our DEM analysis characterizes the continuous temperature distribution of the hot gas and its temporal variation from 2007 to 2021, thus providing up to now the most complete picture on the X-ray evolution of SN 1987A since SN shock encountered with the main ER. We confined our analysis to XMM-Newton observations while not adopting the NuSTAR data, in pursuit of minimizing the systematic uncertainties introduced by different observations from different instruments. However, this leads to a disregarding of the >10 keV spectra. We note that, despite the controversy, based on a simultaneous analysis of the Chandra, XMM-Newton, and NuSTAR data, E. Greco et al. (2021) and E. Greco et al. (2022) suggested that, at >10 keV, the X-ray emission of SN 1987A is dominated by the nonthermal emission from the central PWN. Due to the large column density ($N_{\rm H} > 10^{23}\,{\rm cm}^{-2}$) of the unshocked ejecta, nonthermal emission from the PWN subjected to heavy absorption, and thus has no significant effect to the <10 keV spectra, which is dominated by thermal emission from the shocked hot plasma. Given the fact that our DEM analysis was aimed at the thermal-emitting gas, we expect that disregarding the NuSTAR data will not significantly affect our major conclusions. On the other hand, it is possible that the >10 keV

[9] The time differences between XMM-Newton and NuSTAR observations adopted by D. Alp et al. (2021) for their joint fit are generally around ∼100–200 days, whereas previous studies have shown that the X-ray flux (either broadband flux or line flux) and the surface brightness distribution of SN 1987A vary in a timescale of a few hundred days (e.g., K. A. Frank et al. 2016; L. Sun et al. 2021).

emission is contributed by a high-temperature plasma component, i.e., ∼4 keV as suggested by D. Alp et al. (2021). However, we note that such a high-temperature plasma component has already been characterized in our DEM modeling, even without adopting the NuSTAR data. Nevertheless, a conjoint analysis of RGS + EPIC/Chandra + NuSTAR data may help to set tighter constraints on both the thermal-emitting gas and the nonthermal-emitting PWN, which is of great interest but is out of the scope of this paper.

2. *Spectral model.* The spectral models used in S. A. Zhekov et al. (2006, 2009), D. Alp et al. (2021), and our study are quite similar. The major difference could be that our DEM model is based on the `vnei` model in XSPEC, while previous ones are based on `vpshock`. The `vpshock` model assumes a plane-parallel shock, where the postshock gas has a linear distribution of the ionization parameter τ versus the EM between a lower limit $\tau_{\rm l}$ and an upper limit $\tau_{\rm u}$ (K. J. Borkowski et al. 2001). On the other hand, the `vnei` model characterizes the average property of the plasma with a single temperature $kT_{\rm e}$ and a single ionization parameter τ. Therefore, the `vpshock` model provides a more accurate (but still highly simplified and idealized) description for the plasma whose actual physical condition is (expected to be) close to that under the plane-parallel shock assumption. However, for a complex system such as SN 1987A, the integrated plasma property may significantly deviate from the plane-parallel shock schema with a much more complicated thermalization and ionization history (e.g., as shown by MHD simulations in the first row of Figure 4). In this case, the `vnei` model, although even more simplified compared with `vpshock`, may be more flexible and viable in the sense of providing a general characterization of the average property of the plasma. We have also constructed a DEM model based on `vpshock`, and found that the obtained C statistic and best-fit parameters are similar to those using `vnei`-based DEM model (details on the `vpshock`-based DEM modeling are given in Appendix C). S. A. Zhekov et al. (2006, 2009) restrict the plasma temperature to 0.15–4 keV, which may limit the constraint on high-temperature components. Both S. A. Zhekov et al. (2006, 2009) and D. Alp et al. (2021) adopted a maximum order Chebyshev series $M = 6$ and a total temperature bin number $N = 25$, which in our case are $M = 7$ and $N = 40$ instead. As mentioned in Section 3.1 and detailed in Appendix A, this setup has been optimized for our data through multiple tests and, therefore, may provide better performance. At last, S. A. Zhekov et al. (2006, 2009) was based on a rather old version of the atomic database (the `nei` model version 2.0 in XSPEC version 11.3.2, which is based on AtomDB version 2.0), which is less accurate and may be subjected to some errors.

3. *Procedure.* Neither S. A. Zhekov et al. (2006, 2009) nor D. Alp et al. (2021) presented the verification procedure of the model, and they did not provide the uncertainties (i.e., error bars) of the obtained temperature distributions. We first verified the validity and the reliability of the DEM model through multiple tests as in Section 3.2. In particular, the MHD simulations provide us with a unique opportunity to verify the systematic uncertainty of the DEM model and to identify any artificial features in the results. Then, with an MCMC approach, we obtained not only the best-fit curves but also the 1σ uncertainties of the temperature distributions.

In addition to the major improvements summarized above, there could be other small differences lying in the detailed data processing and analyzing procedures, which may not be fully enumerated. Among all the differences, it is likely that the differences between the data set being used play the most important role in causing the discrepancies in the final results, given that S. A. Zhekov et al. (2006, 2009) and D. Alp et al. (2021) obtained different DEM distributions based on different data set even if they adopted quite similar model configurations.

4.3. Correlation between $\rm n_e t$ and $\rm kT_e$

The hot plasma in SN 1987A is under the NEI state, i.e., the DEM is not only a function of electron temperature $kT_{\rm e}$ but also a function of the ionization parameter $n_{\rm e}t$. Therefore, one of the major challenges in our DEM modeling is how to deal with $n_{\rm e}t$. In order to get a better constraint on the temperature distribution (which is the major objective of this work) and to keep the model as simple as possible, we made the compromise that assumed a simple power-law relation between $n_{\rm e}t$ and $kT_{\rm e}$ (see Equation (3)). However, this assumption, which has also been adopted by S. A. Zhekov et al. (2006, 2009) and D. Alp et al. (2021), might be questionable, given the rather complicated thermal and ionization structure of the plasma.

In the case of shock transmitting into a density gradient, we have $kT_{\rm e} \propto V_{\rm sh}^2 \propto n_{\rm e}^{-1}$, where $V_{\rm sh}$ is the shock velocity. If we assume the plasmas with different densities are shocked at the same time, then there will be a simple relation between temperature and ionization parameters as $kT_{\rm e} \propto (n_{\rm e}t)^{-1}$ (i.e., $\beta = -1$ in Equation (3)).

In collisionless shock heating, the postshock temperatures of different particle species can be different, and the electron–ion temperature ratio can be significantly lower than 1, especially in the case of high-Mach-number shocks (e.g., P. Ghavamian et al. 2007; J. C. Raymond et al. 2023). Observational evidence of this temperature nonequilibrium effect has been found for several SNRs, and especially for SN 1987A (M. Miceli et al. 2019). The postshock electron temperature will then be gradually increased when interacting with other species, and finally get to equilibrium. The increasing rate $dkT_{\rm e}/dt$, taking electron–proton equilibration as an example, is approximately proportional to proton density $n_{\rm p}$ (e.g., J. Vink 2020). Given $n_{\rm p} \approx n_{\rm e}$, in this sense, we got $kT_{\rm e} \propto n_{\rm e}t$ (i.e., $\beta = 1$).

There are still many other mechanisms that may modify the $kT_{\rm e}$–$n_{\rm e}t$ relation, such as adiabatic cooling, thermal conduction, radiative cooling, etc. Furthermore, as revealed by MHD simulations (Figure 4), at different scales and evolution stages, the plasma of different components could be dominated by different mechanisms, making the overall $kT_{\rm e}$–$n_{\rm e}t$ relation extremely complicated. According to simulations, the EM-weighted $n_{\rm e}t$ (Figure 4 middle panels) shows an increase with $kT_{\rm e}$ at very low temperatures ($\lesssim$0.3 keV), a plateau around ∼0.3–1 keV, then a decrease in ∼1–5 keV, and finally an increase again at very high temperatures ($\gtrsim$5 keV). In addition to the complex relation between $n_{\rm e}t$ and $kT_{\rm e}$, the intrinsic

scattering of $n_e t$ is quite large. Therefore, the power-law assumption adopted in the DEM modeling might be over-simplified, and the results must be treated with caution.

Our DEM modeling suggests a flat or positive correlation between $n_e t$ and kT_e (i.e., $\beta \gtrsim 0$) for most of the observations (Figure 2). However, the uncertainties of $n_e t$ are rather large, especially at the lower and higher ends of temperatures. The large uncertainties may be partially due to the poor statistics of the spectra at low and high energy bands. More importantly, it may be caused by the intrinsic scattering of $n_e t$ at each temperature bin, and thus implies the complexity of the ionization history of the plasma. In our DEM modeling, $n_e t$ is constrained mainly based on emission lines—especially those lying in the ∼0.5–2 keV band that are observed and well resolved by RGS. These emission lines are dominated by the plasma within the major peak ($kT_e \sim 0.5$–1 keV). Therefore, despite the large uncertainties at the lower and higher ends of temperatures, the $n_e t$ around ∼0.5–1 keV may still be able to characterize the bulk ionization state of SN 1987A, which is dominated by the shocked ring. On the other hand, the $n_e t$ at 1 keV has been decreasing in the recent few years, which may be associated with the newly shocked ejecta that lowers the average ionization state of the plasma.

4.4. Latest Evolution of the Fe K Line and Its Implications to Newly Shocked Ejecta Materials

The newly shocked ejecta that are uncovered by our DEM analysis as well as the MHD simulation can also be supported by the recent changes of the Fe K line centroid. The Fe K complex contains a series of Fe K-shell fluorescent lines, where the line energy rises slowly in the range of ∼6.4–6.7 keV as a function of the ionization state (e.g., Figure 12 in J. Vink 2012). The emission from individual ion species can hardly be resolved, and the whole Fe K complex usually appears as one single emission line in the CCD spectrum. The centroid energy of this Fe K line is thereby determined by the contributions of different ions, and thus may represent the average temperature and ionization parameters of Fe (e.g., Figure 10 in L. Sun et al. 2021).

The Fe K line has been detected from SN 1987A using different instruments (e.g., R. Sturm et al. 2010; P. Maggi et al. 2012; D. Alp et al. 2021; L. Sun et al. 2021; C. Maitra et al. 2022; A. P. Ravi et al. 2024). In particular, L. Sun et al. (2021) found both the flux and the centroid energy of the Fe K line have been increasing from 2007 to 2019. Here, we update the latest variations of the Fe K line based on new XMM-Newton EPIC-pn observations taken in 2020 and 2021. As shown in Figure 6, the flux of the Fe K line was still increasing, corresponding to the increasing EM of the high-temperature plasma. On the other hand, we found a moderate decline of the centroid energy from ∼6.65–6.7 to $\lesssim$6.60 keV in the last few years (see Appendix D for a detailed investigation on the statistical significance), which implies the average ionization state of Fe might have been decreasing recently. As shown by L. Sun et al. (2021), the temporal evolution of the Fe K centroid energy before 2019 can be well described by a plasma component with a temperature $kT_e = 3.2$ keV and a density $n_e = 500\,\mathrm{cm}^{-3}$, shocked at ∼7000 days after the explosion, seen as the gray dashed curve in Figure 6. The recent drop-off in ionization state deviates from this scenario and indicates that a newly shocked plasma component may have contributed to the Fe K emission.

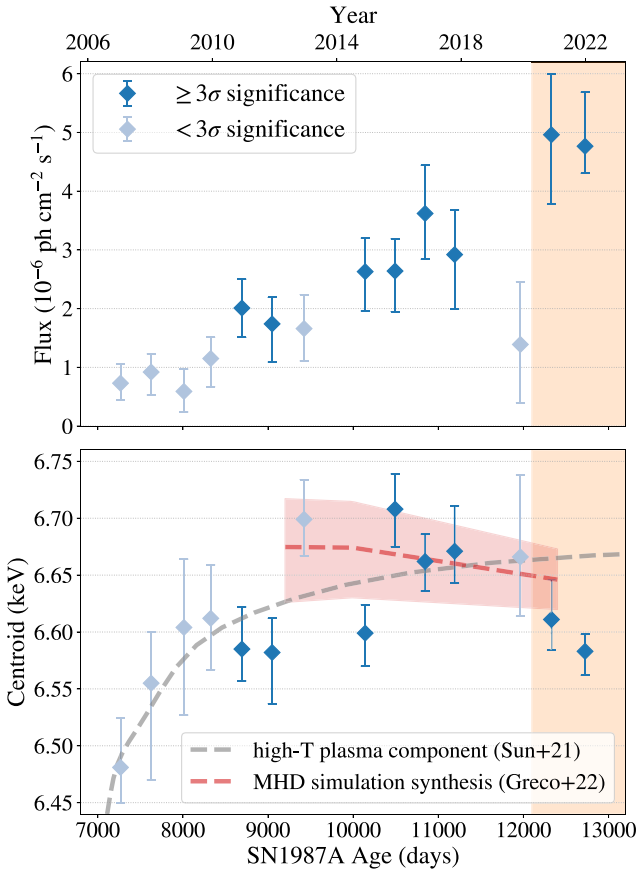

Figure 6. Light curve (upper panel) and centroid energy evolution (lower panel) of the Fe K line from SN 1987A. Data points before 2019 are adopted from L. Sun et al. (2021), while the last two are new results (highlighted with orange areas). Points with $\gtrsim 3\sigma$ detection are shown in dark blue, while the others in light blue. The gray dashed curve is adopted from L. Sun et al. (2021), which represents the Fe K centroid energy for a high-temperature plasma component with $kT_e = 3.2$ keV and $n_e = 500\,\mathrm{cm}^{-3}$, shocked at 7000 days after the explosion. The red dashed curve indicates the MHD simulation predicted centroid energy, obtained by fitting the synthetic spectra evaluated by E. Greco et al. (2022).

E. Greco et al. (2022) presented a detailed discussion on the origins of the Fe K line (see Section 3 and Figure 4 therein). Contributions from different components (i.e., the ER, the ejecta, and the H II region) at different epochs have been evaluated based on the MHD simulations from S. Orlando et al. (2020). The simulations suggest that the Fe K emission is first dominated by the shocked ring, especially by the lower-density material lying between the dense clumps, at around 2012. Then, the contribution from the shocked ejecta gradually increases, which becomes comparable with the ring at around 2020 and will finally dominate the Fe K emission in the near future. Since the newly shocked ejecta has a lower average ionization parameter than the ring, this will result in a decline of the Fe K line centroid energy. This is demonstrated by the red dashed line in Figure 6, which is obtained by fitting the synthetic spectra evaluated by E. Greco et al. (2022). We found the MHD simulation synthesis that involves the complex constitution of the Fe-K-emitting gas, especially the recently shocked ejecta, can be better compared to observations.

In summary, we found a moderate decrease of the Fe K centroid energy in the last few years, which can be well explained by simulations, and thus may provide another

observational evidence for the brightening of the shocked ejecta, in addition to the DEM results.

A. P. Ravi et al. (2024) measured the fluxes and centroid energies of the Fe K line from 2018 to 2022 using Chandra ACIS observations (see their Table 2 and Figure 6). They found the Fe K flux has significantly increased since 2018, from $\sim 4 \times 10^{-6}$ ph cm^{-2} s^{-1} (2018 March) to $\sim 9 \times 10^{-6}$ ph cm^{-2} s^{-1} (2022 September), with typical uncertainties of ∼30%. They obtained an average centroid energy in 2018–2022 as ∼6.66 keV. Despite the large uncertainties, the centroid energies measured in 2020 and 2022 (6.63 ± 0.09 keV and 6.61 ± 0.05 keV, respectively) seem to be lower than those measured in 2018–2019 (∼6.7 keV). Nevertheless, no statistically significant variation can be possibly addressed. Their results on Fe K line flux and centroid energy are generally in agreement with ours. The plausible recent decrease in centroid energy has not been revealed by Chandra observations, but should be continuously monitored and further investigated in future works.

5. Summary and Conclusions

We performed a comprehensive DEM analysis on the X-ray emitting gas in SN 1987A from 2007 to 2021 based on XMM-Newton RGS + EPIC-pn observations. We obtained the continuous temperature distribution of SN 1987A and followed its up-to-date evolution. Our results make it possible to compare the observed temperature structure directly with those predicted by MHD simulations, and by doing that, we found an excellent consistency between observations and simulations. Based on this consistency, we identified a recent brightening of the reverse shock-heated ejecta component and confirmed the fading of the ER. The main results and conclusions of this work are summarized below.

1. The X-ray plasma in SN 1987A followed a similar temperature distribution from 2007 to 2021, which consists of a major peak at ∼0.5–1 keV and a tail to the high-temperature end (up to $\gtrsim$5 keV).
2. The major peak gradually moved from ∼0.5 to ∼1 keV, indicating an increase in the average temperature. The total EM of this peak kept climbing in the first few years, reached its maximum at around 2011–2014, and then started to decline. On the other hand, the high-temperature tail shows a continuous increase in its EM and seems to have formed a secondary peak at ∼3–5 keV in the recent few years.
3. The DEM results show good consistency with the MHD simulation predictions, in all the following aspects: the temperature and EM of the major peak, the existence of a high-temperature tail and its extent, and the overall evolution of the DEM profile. By comparing observations with simulations, we argue that the recent decline of the major peak and the rapid rising of the tail (the emergence of a secondary peak) reveal the fading of the ER and the brightening of the shocked ejecta.
4. We did not find a recent increase in the average metal abundance of SN 1987A. On the contrary, after a plateau around 2009–2016 (∼8000–11,000 days), the abundances have been gradually decreasing and recently got back to the level as they were around 2007 (∼7000 days). We interpret this result as evidence that the forward shock has left the main ER (with higher metal abundances; L. Sun et al. 2021), while the reverse shock has not yet reached the metal-rich inner ejecta.
5. We found a moderate decline of the centroid energy of the Fe K line from ∼6.65–6.7 to $\lesssim$6.6 keV in the recent few years, implying a decrease in the average ionization level of Fe. This is consistent with MHD simulations, which predict the Fe line emission to be more and more contributed by the newly shocked outermost ejecta with a lower ionization parameter (and abundances similar to those of the CSM), and thus may provide additional evidence for the brightening of the outermost layers of ejecta.

This work shows again the great importance of SN 1987A as a representative SN/SNR in the sense of linking observations with simulations. We hope the future multiwavelength monitoring of SN 1987A, and the high-resolution X-ray spectroscopic studies using XRISM, HUBS, LEM, etc., will continuously deepen our insight into this fascinating object and the underlying physics.

Acknowledgments

L.S. and Y.C. acknowledge the NSFC fundings under grants 12173018, 12121003, and 12393852. L.S. acknowledges the support from Jiangsu Funding Program for Excellent Postdoctoral Talent (2023ZB252). P.Z. is thankful for the support from NSFC grant No. 12273010. S.O., E.G., and M.M. acknowledge financial contribution from the PRIN 2022 (20224MNC5A)—"Life, death and after-death of massive stars" funded by European Union—Next Generation EU, and the INAF Theory Grant "Supernova remnants as probes for the structure and mass-loss history of the progenitor systems."

Software: XSPEC (K. A. Arnaud 1996), SPEX (J. S. Kaastra et al. 1996), SAS (C. Gabriel et al. 2004).

Appendix A
Selection of the DEM Model Parameter *M* and *N*

As mentioned in Section 3.1, the maximum order of the Chebyshev series M and the total temperature bin number N may affect the fitting results. We thereby optimized the selection of M and N by experimenting with various configurations to evaluate their performance. In this section, we present several test cases utilizing different M and N configurations (as shown in Figure 7). For instance, by setting $M = 6$ and $N = 25$, we found that it yields acceptable fits for the 1-T and 2-T test models (Figures 7(a) and (b)). However, it fails to distinctly resolve the individual components in the 3-T test, where the three peaks (corresponding to three delta functions in the theoretical model) are conflated with each other (Figure 7(c)). It also significantly overestimates the temperatures of the 1 and 4 keV components, resulting in two peaks around 1.2–1.3 and 6–7 keV. Increasing M to 7 improves the fit and helps to better resolve the three components. However, the low- and middle-temperature components remain inadequately separated (Figure 7(d)), and the overestimation on temperatures remains notable (the high-temperature component is now lying in 5–6 keV, a little bit closer to its theoretical value compared with $M = 6$). When adopting $M = 7$ and $N = 40$ (as illustrated by Figure 1 in Section 3.2), all three peaks can be clearly distinguished. the discrepancies between the estimated and theoretical temperatures are now acceptable (up to ∼10% at

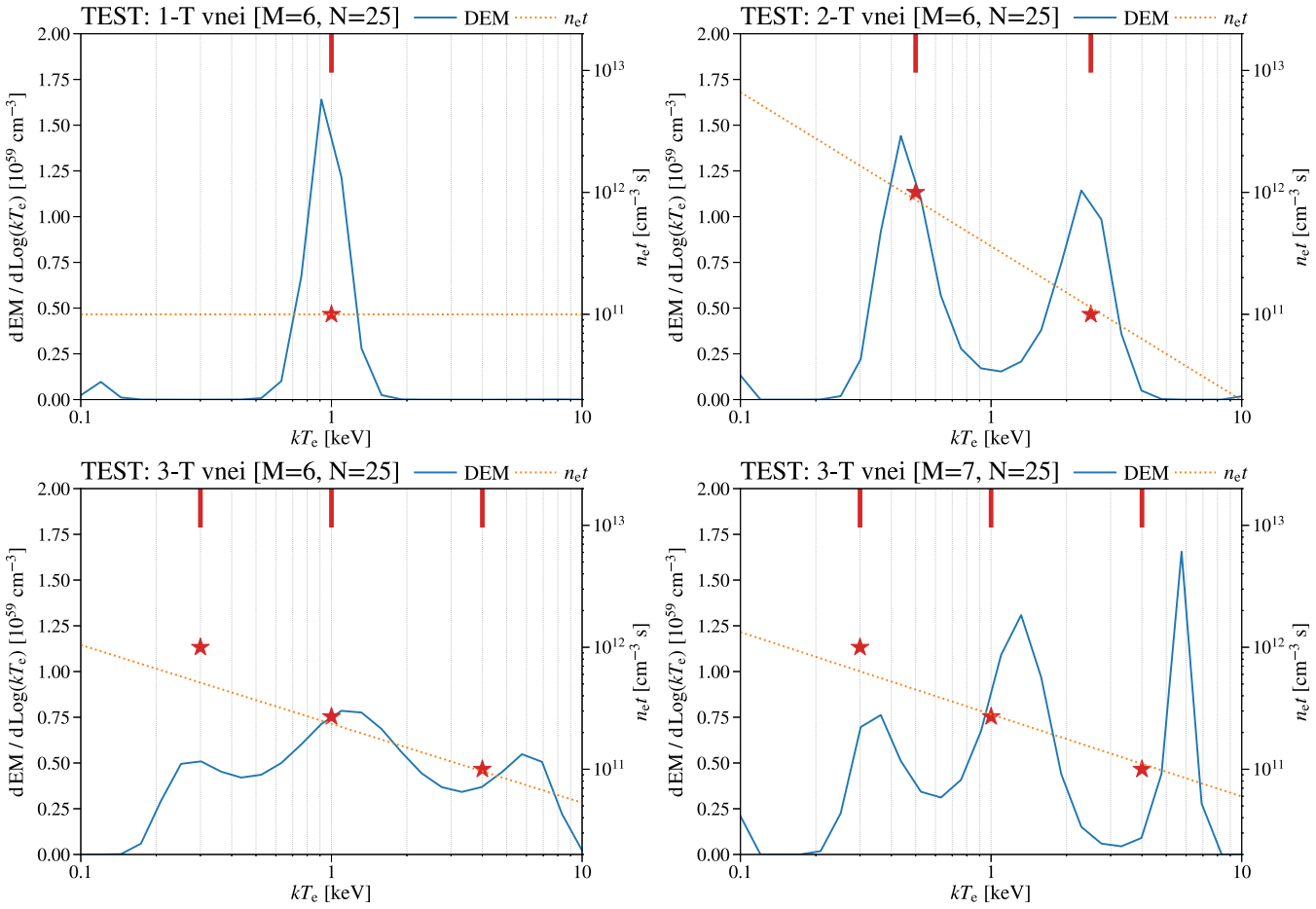

Figure 7. Similar to Figure 1, but adopting different M, N configurations. The blue solid curves denote the best-fit DEM distributions, and the orange dotted lines denote the best-fit ionization parameter distributions. The red lines and stars denote the temperature and ionization parameters used in theoretical models. (a) $M = 6$, $N = 25$ DEM model fit to 1-T `vnei` test spectra; (b) $M = 6$, $n = 25$ DEM model fit to 2-T `vnei` test spectra; (c) $M = 6$, $N = 25$ DEM model fit to 3-T `vnei` test spectra; (d) $M = 7$, $N = 25$ DEM model fit to 3-T `vnei` test spectra.

1 keV and up to ∼25% at 4 keV, which are taken as systematic uncertainties and will not affect our final conclusions). We have also explored even larger values for M and N (e.g., $M = 8$ and $N = 60$) in pursuit of enhanced resolution capabilities. Nevertheless, the improvements are marginal. Specifically, fine structures such as those in simulated DEMs cannot be fully resolved regardless of how much we increase M and N, and the systematic uncertainties of temperature estimation will not be significantly reduced. On the other hand, the computational times for spectral fitting and MCMC running escalate significantly as M and N increase. As a result, we selected $M = 7$ and $N = 40$ as the most efficient configurations for our DEM modeling.

Appendix B
Detailed DEM Fitting Results and MCMC Corner Plots

In this appendix, we provide the detailed fitting results (i.e., best-fit parameters and their 1σ errors) together with the MCMC corner plots and the fitted spectra for our DEM modeling (Figures 8–21).

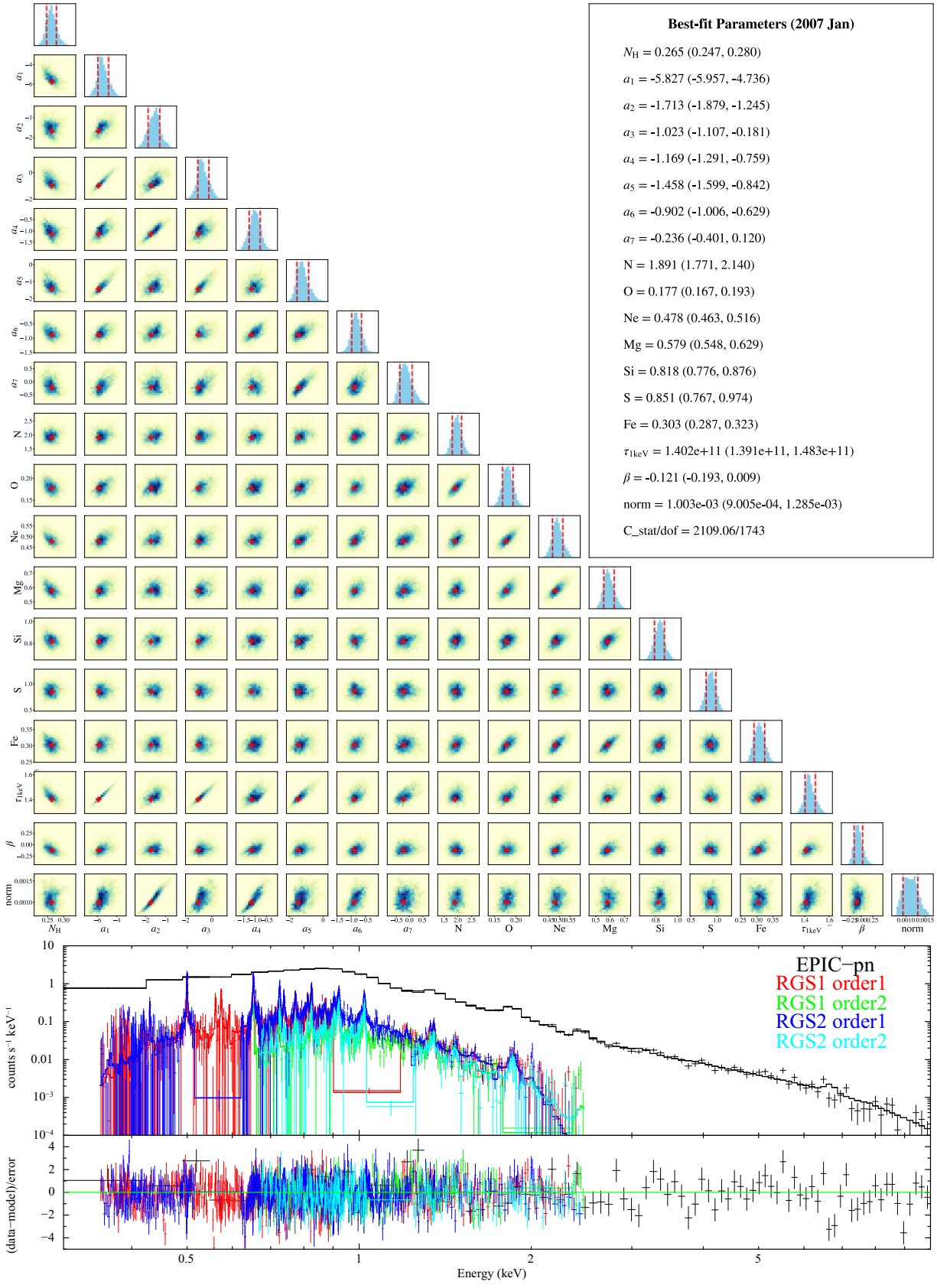

Figure 8. DEM fitting results, MCMC corner plots, and the fitted spectra for the observation taken in 2007 January. The values of N_H, $\tau_{1\ keV}$, and norm (defined as $10^{-14}/(4\pi d^2)\int n_e n_H dV$, where d is the distance to SN 1987A and V the emitting volume) are in units of 10^{22} cm^{-2}, cm^{-3} s, and cm^{-5}, respectively.

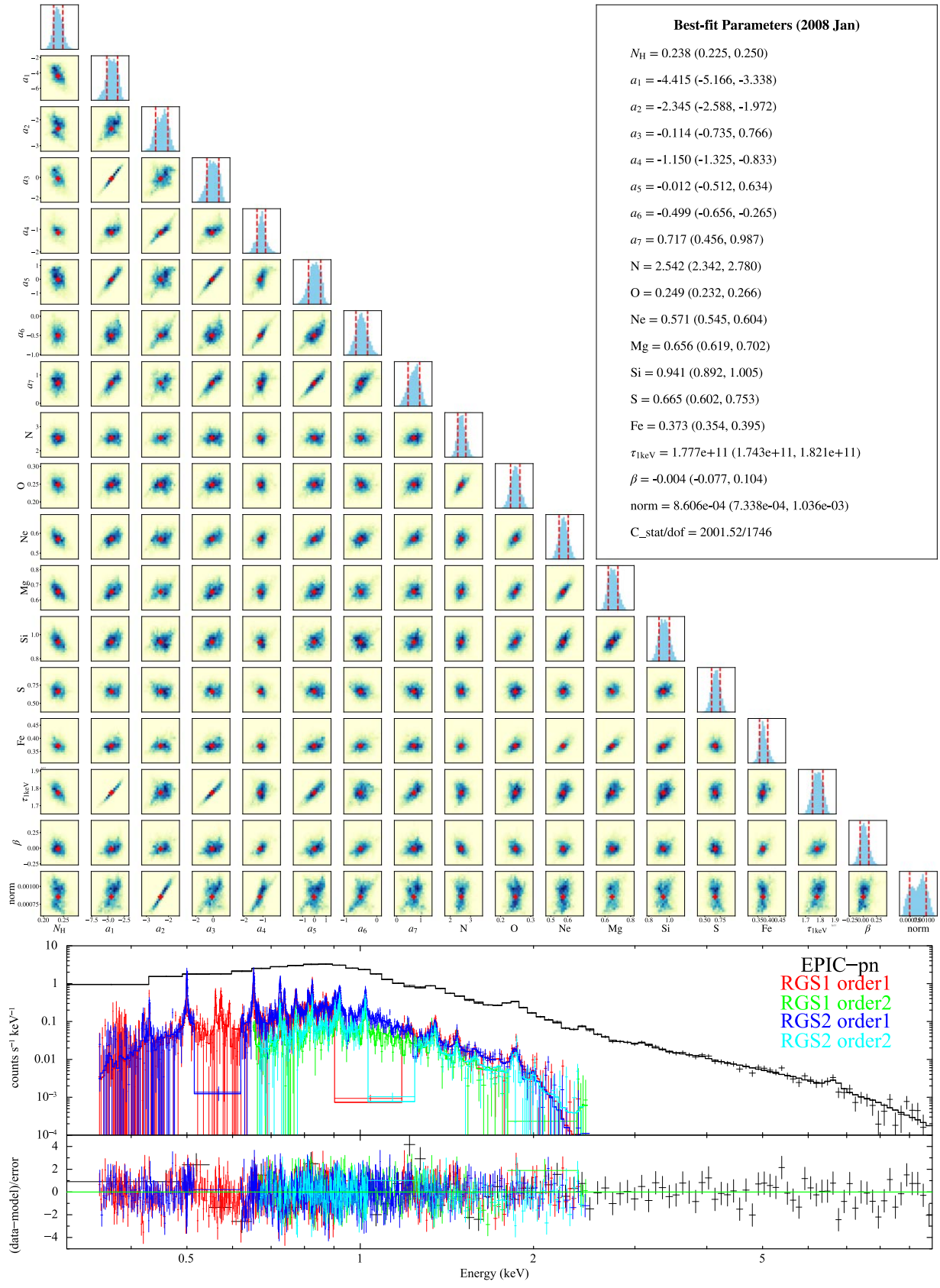

Figure 9. Same as Figure 8, but for the observation taken in 2008 January.

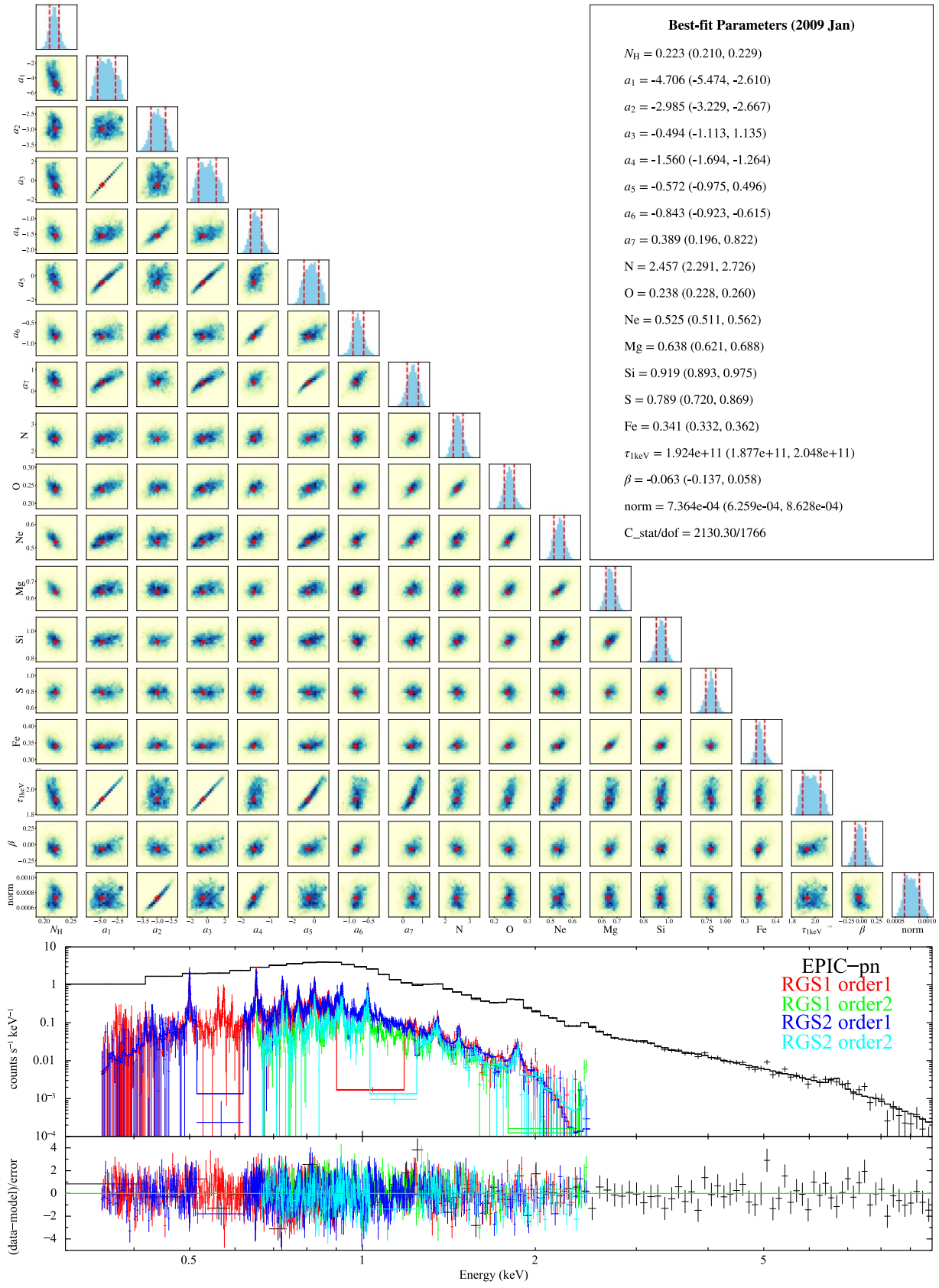

Figure 10. Same as Figure 8, but for the observation taken in 2009 January.

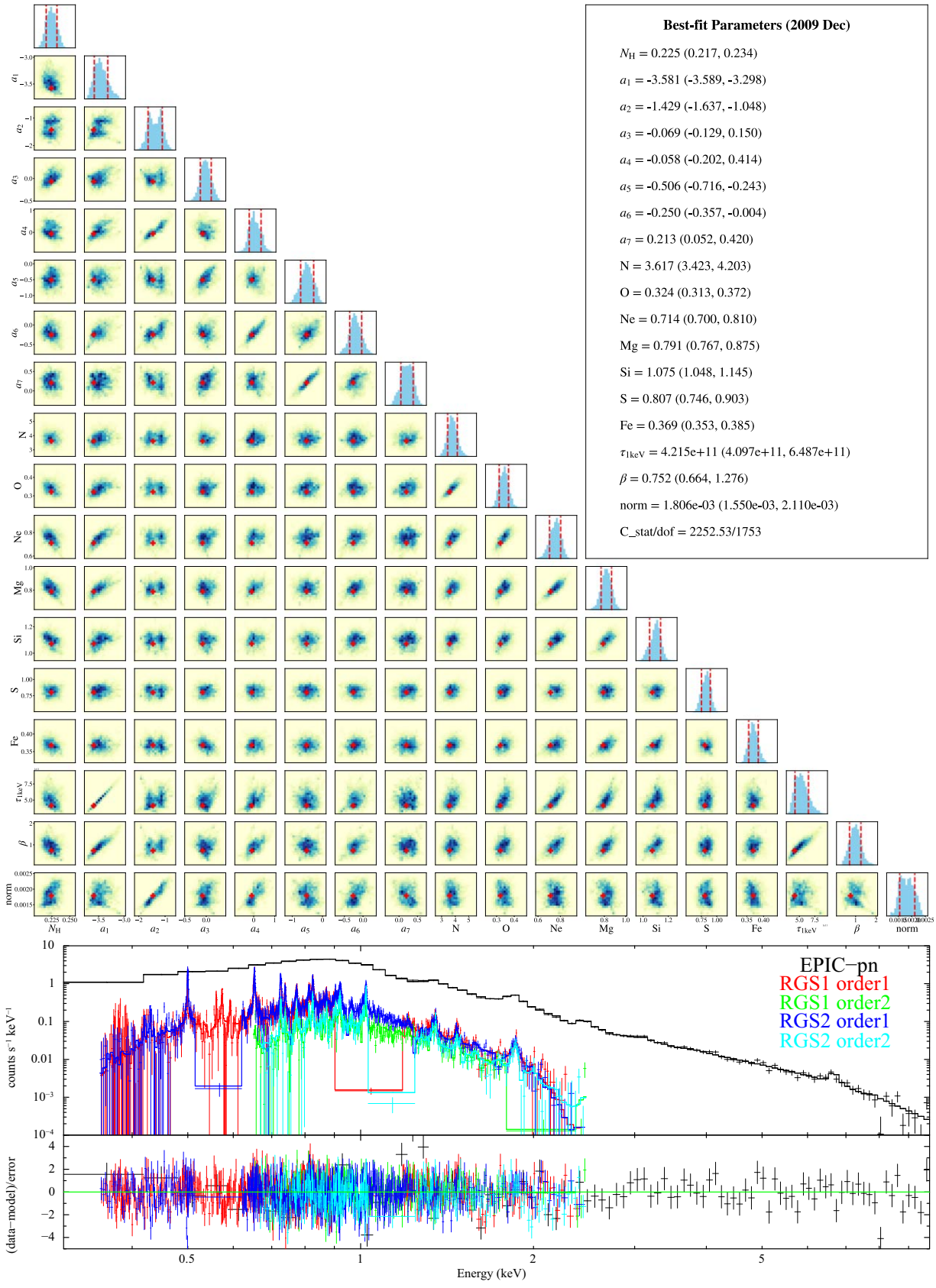

Figure 11. Same as Figure 8, but for the observation taken in 2009 December.

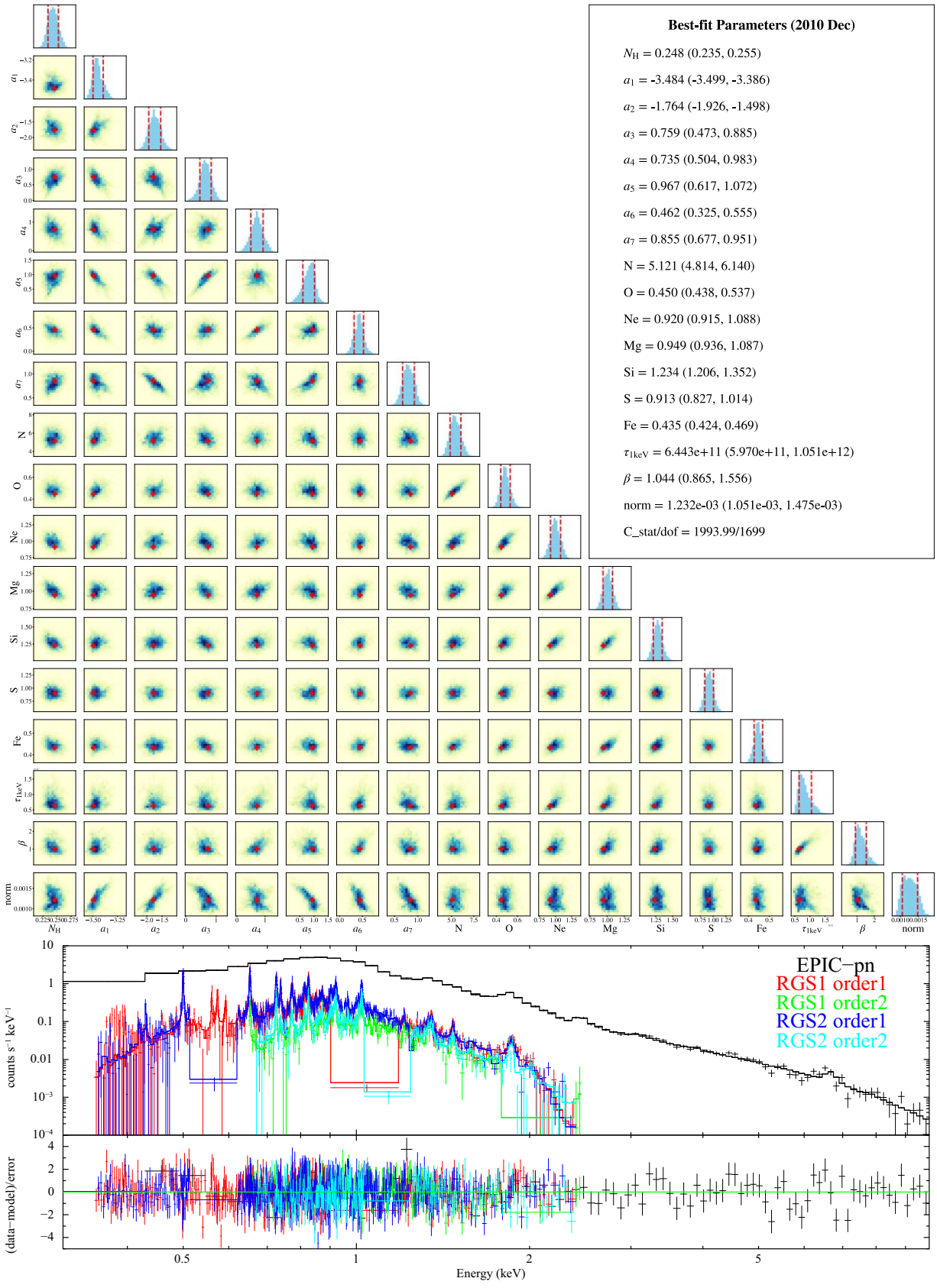

Figure 12. Same as Figure 8, but for the observation taken in 2010 December.

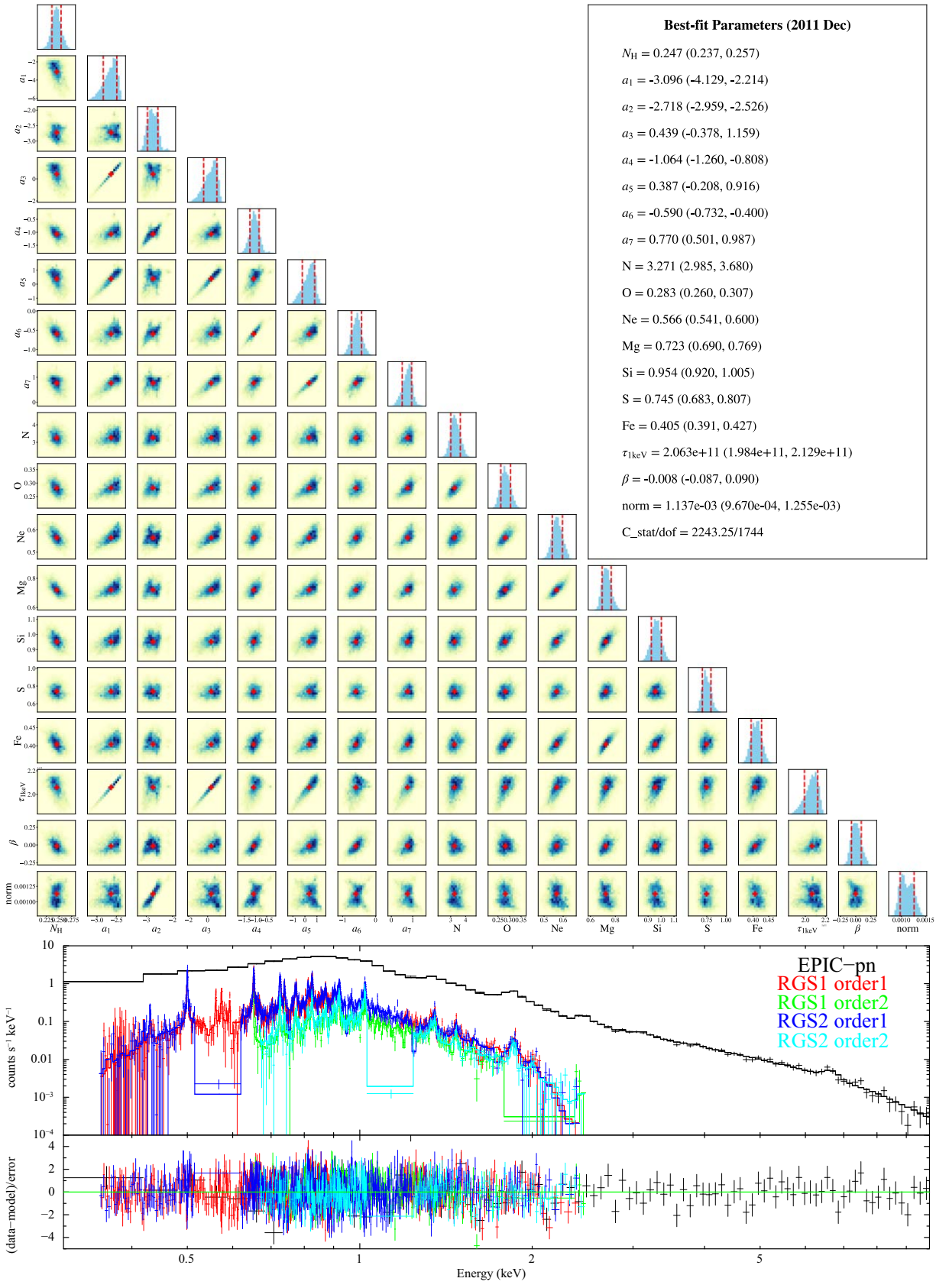

Figure 13. Same as Figure 8, but for the observation taken in 2011 December.

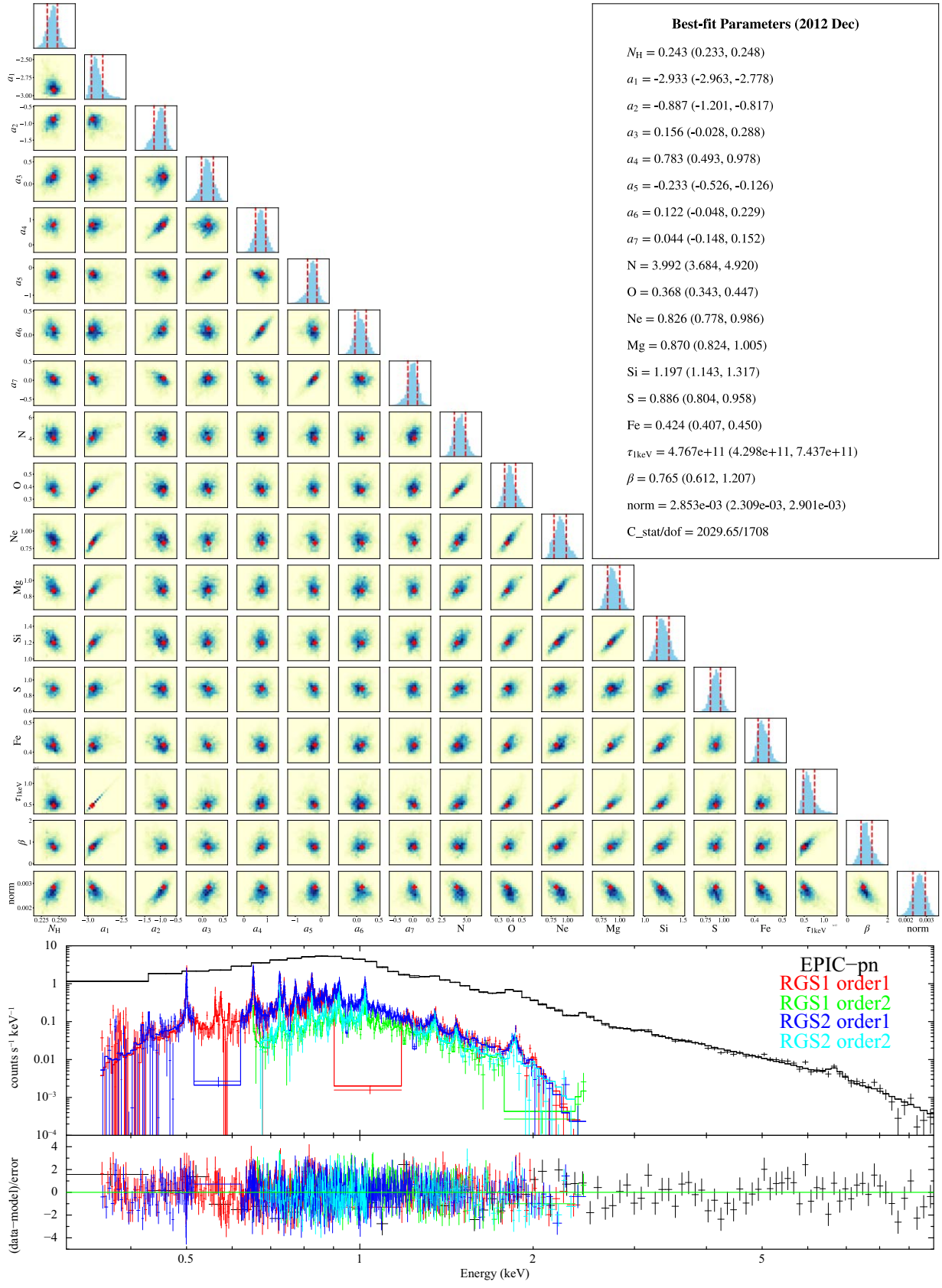

Figure 14. Same as Figure 8, but for the observation taken in 2012 December.

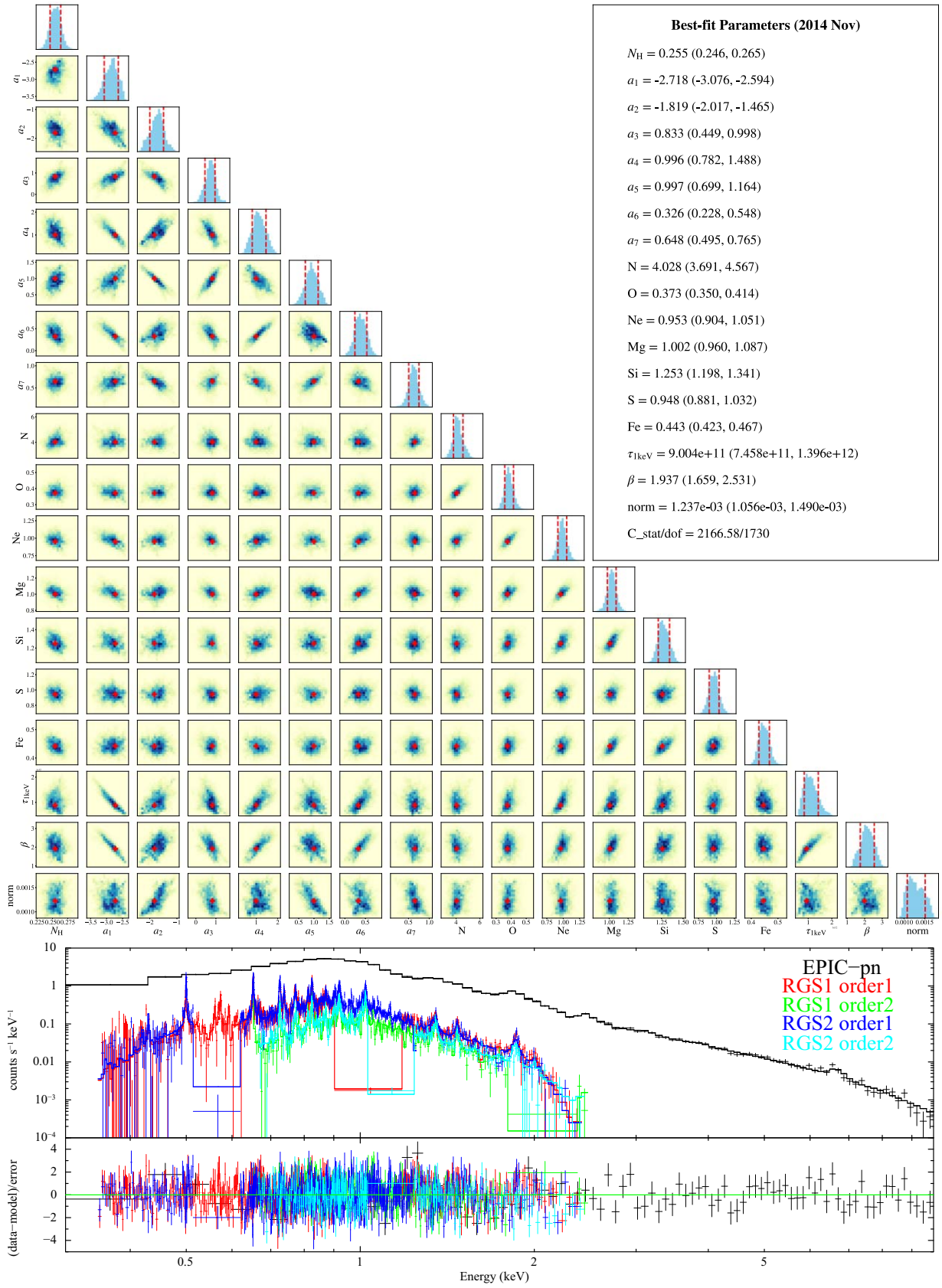

Figure 15. Same as Figure 8, but for the observation taken in 2014 November.

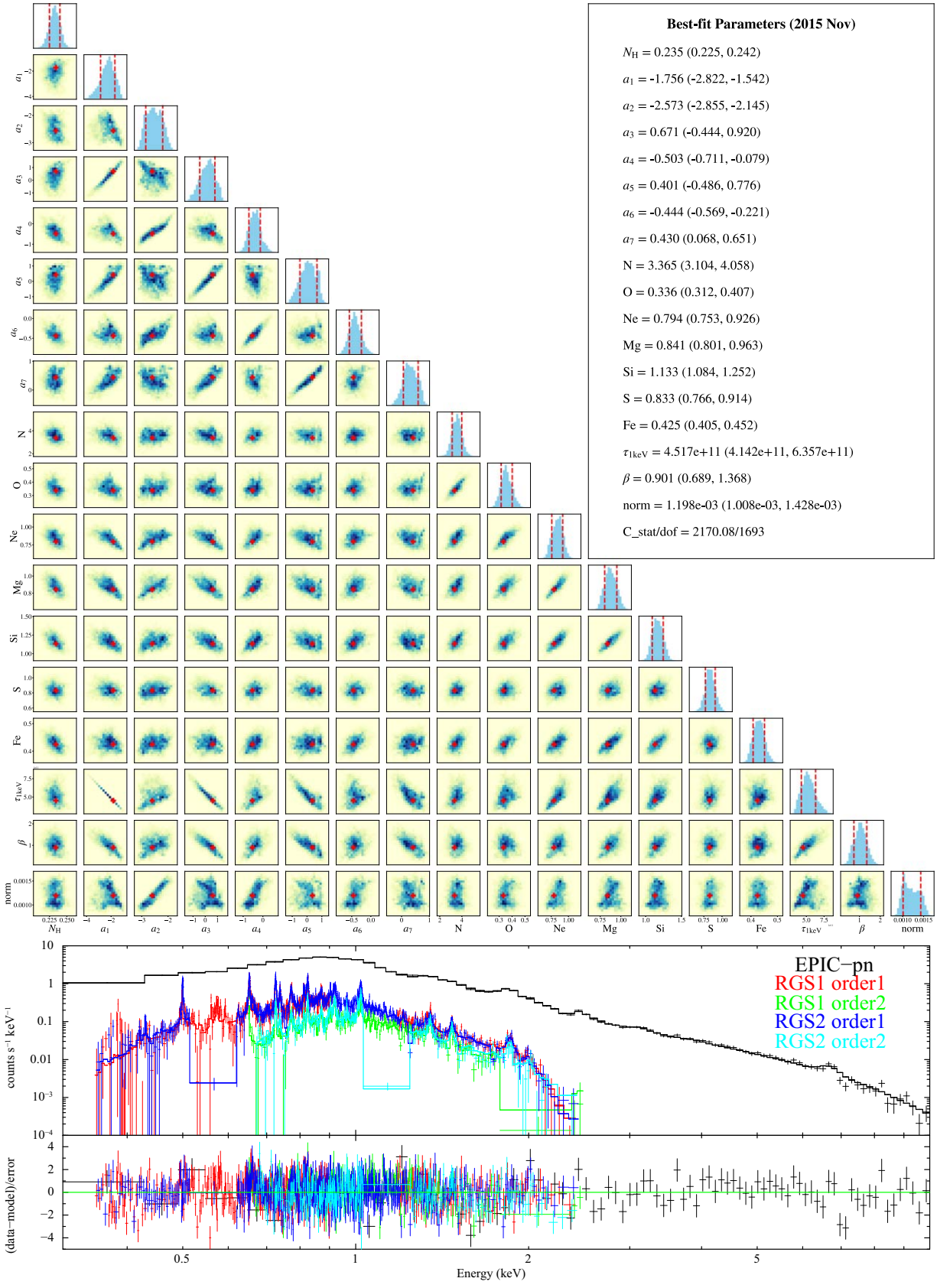

Figure 16. Same as Figure 8, but for the observation taken in 2015 November.

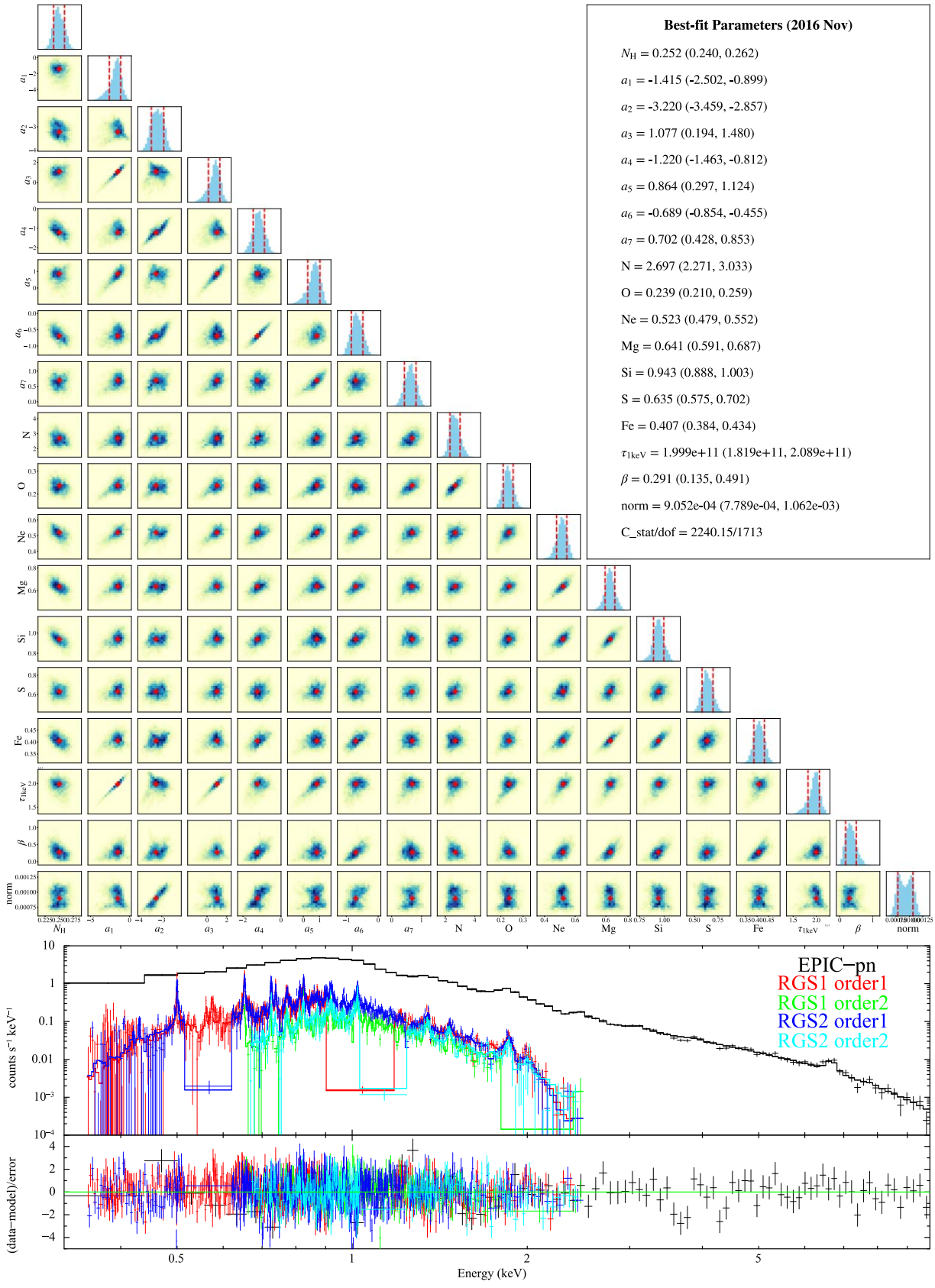

Figure 17. Same as Figure 8, but for the observation taken in 2016 November.

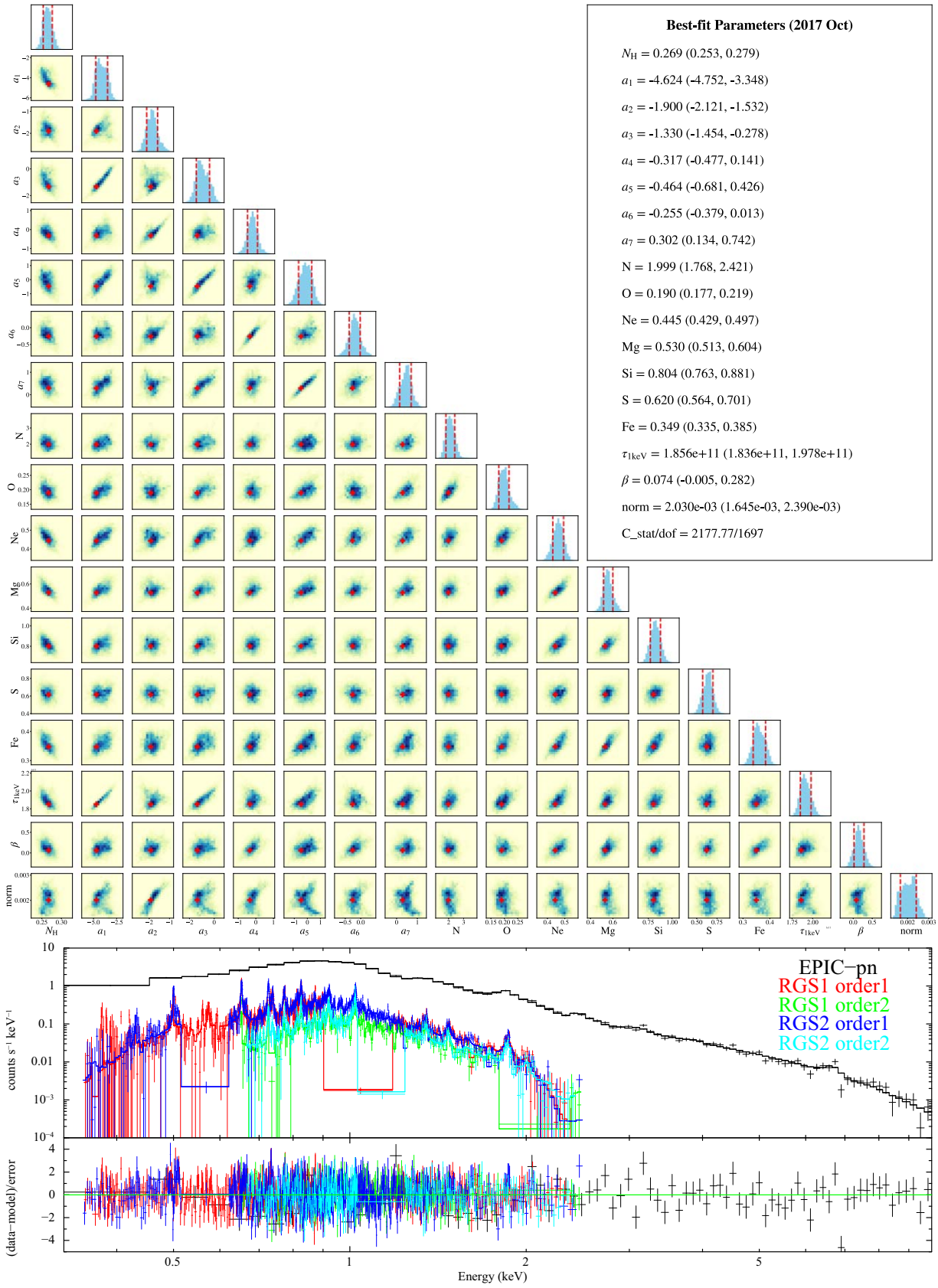

Figure 18. Same as Figure 8, but for the observation taken in 2017 October.

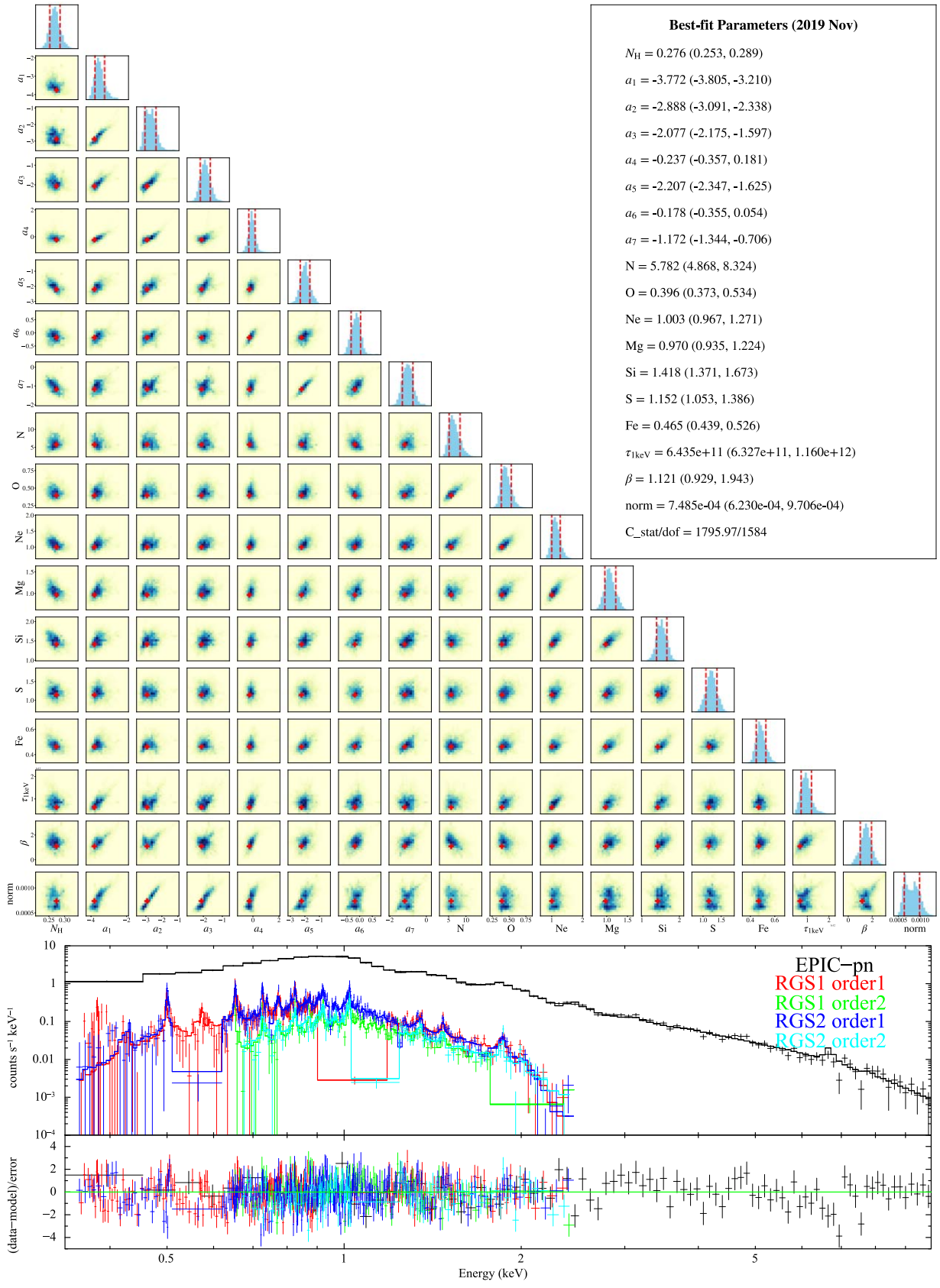

Figure 19. Same as Figure 8, but for the observation taken in 2019 November.

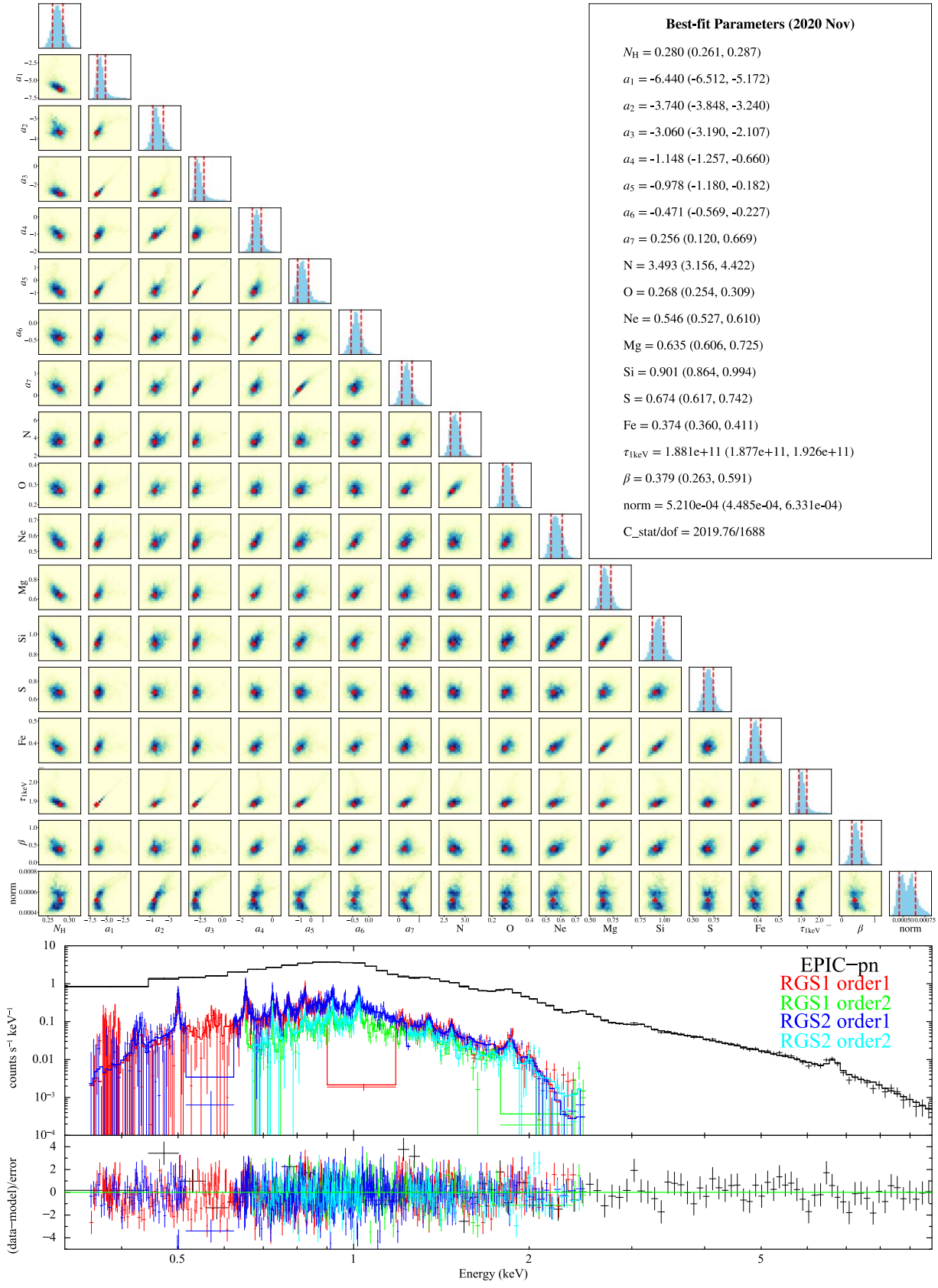

Figure 20. Same as Figure 8, but for the observation taken in 2020 November.

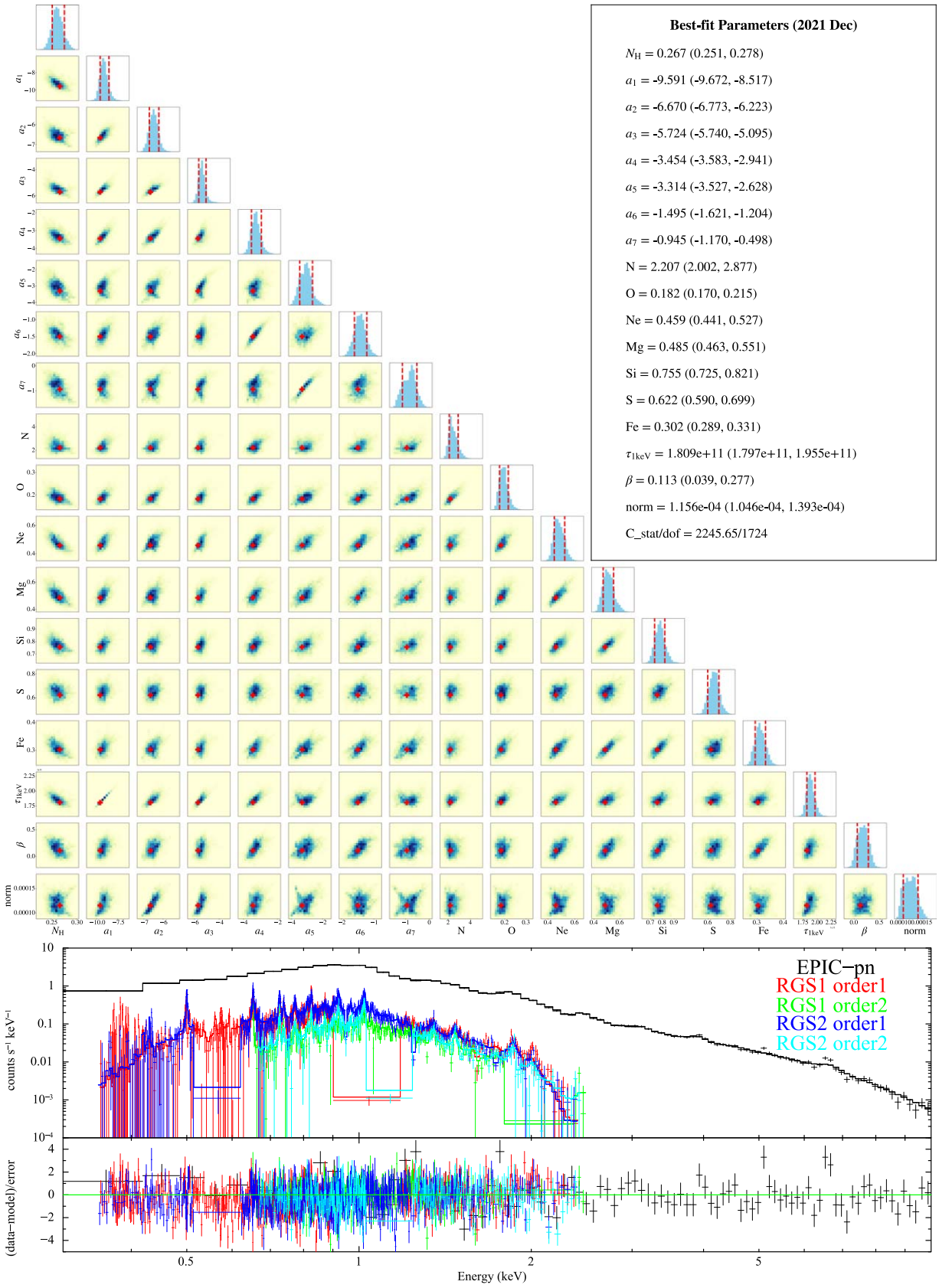

Figure 21. Same as Figure 8, but for the observation taken in 2021 December.

Appendix C
DEM Analysis Results Based on the vpshock Model

Despite the disadvantages with respect to vnei-based DEM modeling as illustrated in Section 4.2, we constructed a DEM model based on the vpshock model in XSPEC analogous to the vnei-based model as described in Section 3.1, in order to compare their results. We applied this vpshock-based DEM model to the RGS + EPIC-pn data of SN 1987A. The fitting results (i.e., the best-fit DEM and $n_e t$ with their 1σ errors as a function of kT_e) are shown in Figure 22. Similar to the vnei-based fitting, vpshock-based DEM modeling also revealed a major peak and a high-temperature tail in the DEM distribution

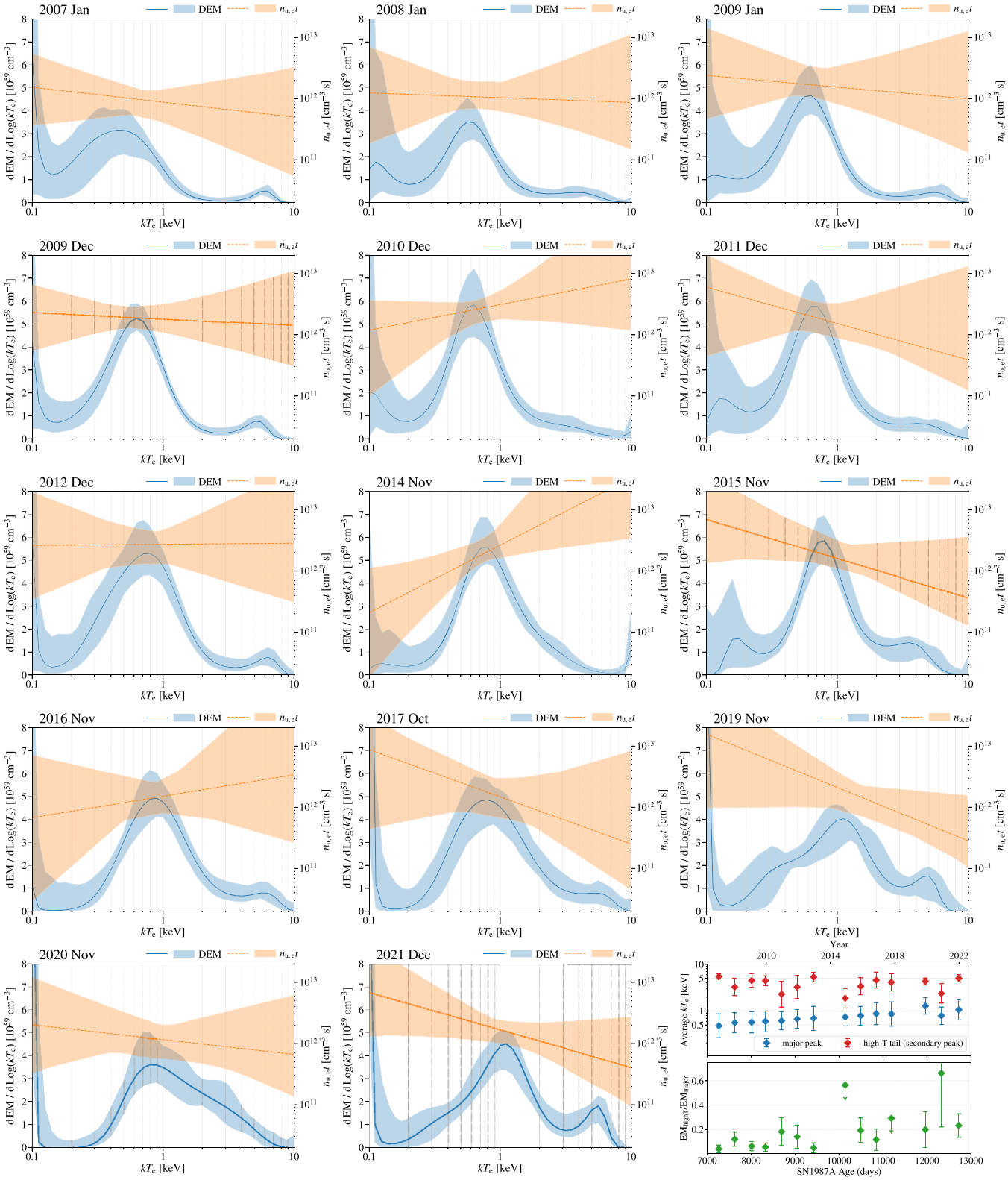

Figure 22. DEM fitting results for SN 1987A based on the vpshock model.

of SN 1987A, and captured the temporal evolution of their average temperatures and EMs. The average temperature of the major peak gradually increased from ∼0.5 to ∼1 keV. A recent rising of the high-temperature tail can also be seen in the vpshock-based fitting, resulting in an increase in the EM ratio EM_{highT}/EM_{major}.

The most prominent difference between the vpshock-based and vnei-based DEM modeling is in the obtained ionization parameter distributions. The ionization parameters obtained by the vpshock-based modeling appear to be generally higher than those obtained by vnei-based modeling, which is because the $n_{u,e}t$ in vpshock model is defined as the upper limit of the ionization parameter rather than the average value n_et in vnei. In contrast with the average n_et given by vnei-based fitting showing a positive relation with temperature, $n_{u,e}t$ given by vpshock-based fitting exhibits a flat or negative relation with kT_e (i.e., $\beta \lesssim 0$ in Equation (3)). Despite the rather large uncertainties, this may indicate that, for the high-temperature gas, the average ionization parameter is closer to its upper limit, while for the low-temperature gas, even though the upper limit of the ionization parameter is rather high, its average value is still low. This is consistent with the findings of L. Sun et al. (2021) based on 2-T vnei and vpshock fitting, and might imply the different ionization histories of the high- and low-temperature gas.

Appendix D
Statistical Significance of the Recent Decrease in Fe K Centroid Energy

In order to approximately evaluate the statistical significance of the recent decrease in centroid energy of the Fe K line, we followed the subsequent procedures.

First, we assumed that the centroid energy remains constant (at the average value) throughout the entire period (2007–2021) and calculated the chi-squared. We obtained the $\chi^2/\mathrm{dof} \sim 40.8/13$, corresponding to p-value $\sim 1 \times 10^{-4}$, suggesting that the centroid energy is not likely to be constant throughout the entire period.

Subsequently, we fitted the observed centroid energies from 2007 to 2019 (excluded the last two data points) using a piecewise linear function with two segments. This model provides a good fit to the Fe K centroid energy from 2007 to 2019, with a $\chi^2/\mathrm{dof} \sim 12.1/8$. The best-fit result is presented as the red dashed curves in the left panel of Figure 23 (the 1σ, 2σ, 3σ uncertainty ranges are denoted by the shaded regions). The fitting result indicates a fast increase of Fe K centroid energy before ∼8000 days after the explosion, followed by a slower increase until ∼12,000 days. If we extrapolate the best-fit curve and the uncertainty ranges to 2021, we found that the two new observations show a significant deviation from the best fit, which fall out of the 3σ region, indicating a recent decrease in Fe K centroid energy. However, we noted that some of the 2007–2019 observations also show large scatterings from the best-fit curve, lying outside the 3σ region (e.g., 2012, 2014, and 2015).

At last, we fitted the observations in the entire period (2007–2021, including the last two data points) with piecewise linear functions. We first assumed that there is no decrease—the centroid energy increased at the beginning, and then keeps constant after some point. The best-fit result in this case (without decrease) is shown as the gray dashed line in the right panel of Figure 23, which gives a $\chi^2/\mathrm{dof} \sim 25.6/10$. Then, we introduced a recent decrease into the fitting model. The best-fit result in this case (with decrease) is shown as the red dashed line, which gives a $\chi^2/\mathrm{dof} \sim 12.1/8$. An F-test between the two models gives p-value ∼0.0497, which suggests that the with-decrease model is favored at a $\sim 2\sigma$ significance level.

Given the investigations above, we considered the recent decrease in Fe K centroid energy to be moderately significant ($\sim 2\sigma$–3σ level).

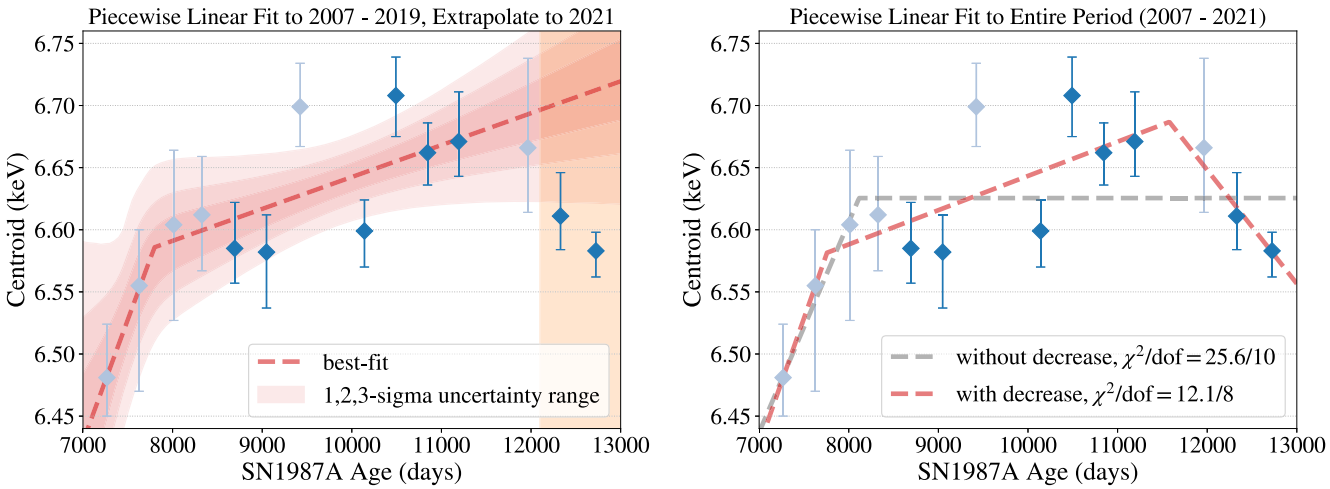

Figure 23. Piecewise linear fit to the Fe K centroid energy. Left: fit to the observations from 2007 to 2019, and then, extrapolate the result to 2021. The red dashed line denotes the best-fit model, and the shaded regions indicate the 1σ, 2σ, and 3σ uncertainty ranges. Right: fit to the entire period (2007 to 2021). The gray dashed line denotes the best-fit model without a recent decrease, while the red dashed line denotes the best-fit model with a recent decrease.

ORCID iDs

Lei Sun https://orcid.org/0000-0001-9671-905X
Salvatore Orlando https://orcid.org/0000-0003-2836-540X
Emanuele Greco https://orcid.org/0000-0001-5792-0690
Marco Miceli https://orcid.org/0000-0003-0876-8391
Yang Chen https://orcid.org/0000-0002-4753-2798
Jacco Vink https://orcid.org/0000-0002-4708-4219
Ping Zhou https://orcid.org/0000-0002-5683-822X

References

Alp, D., Larsson, J., & Fransson, C. 2021, ApJ, 916, 76
Arendt, R. G., Dwek, E., Bouchet, P., et al. 2016, AJ, 151, 62
Arnaud, K. A. 1996, in ASP Conf. Ser. 101, Astronomical Data Analysis Software and Systems V, ed. G. H. Jacoby & J. Barnes (San Francisco, CA: ASP), 17
Borkowski, K. J., Lyerly, W. J., & Reynolds, S. P. 2001, ApJ, 548, 820
Bray, E., Burrows, D. N., Park, S., & Ravi, A. P. 2020, ApJ, 899, 21
Buote, D. A. 2000, MNRAS, 311, 176
Castor, J., McCray, R., & Weaver, R. 1975, ApJL, 200, L107
Dewey, D., Dwarkadas, V. V., Haberl, F., Sturm, R., & Canizares, C. R. 2012, ApJ, 752, 103
Frank, K. A., Zhekov, S. A., Park, S., et al. 2016, ApJ, 829, 40
Fransson, C., Barlow, M. J., Kavanagh, P. J., et al. 2024, Sci, 383, 898
Fransson, C., Larsson, J., Migotto, K., et al. 2015, ApJL, 806, L19
Fransson, C., Larsson, J., Spyromilio, J., et al. 2013, ApJ, 768, 88
Gabriel, C., Denby, M., Fyfe, D. J., et al. 2004, in ASP Conf. Ser. 314, Astronomical Data Analysis Software and Systems (ADASS) XIII, ed. F. Ochsenbein, M. G. Allen, & D. Egret (San Francisco, CA: ASP), 759
Ghavamian, P., Laming, J. M., & Rakowski, C. E. 2007, ApJL, 654, L69
Greco, E., Miceli, M., Orlando, S., et al. 2021, ApJL, 908, L45
Greco, E., Miceli, M., Orlando, S., et al. 2022, ApJ, 931, 132
Greco, E., Vink, J., Miceli, M., et al. 2020, A&A, 638, A101
Haberl, F., Geppert, U., Aschenbach, B., & Hasinger, G. 2006, A&A, 460, 811
Heng, K., Haberl, F., Aschenbach, B., & Hasinger, G. 2008, ApJ, 676, 361
Kaastra, J. S., & Bleeker, J. A. M. 2016, A&A, 587, A151
Kaastra, J. S., Mewe, R., & Nieuwenhuijzen, H. 1996, in 11th Coll. on UV and X-ray Spectroscopy of Astrophysical and Laboratory Plasmas, ed. K. Yamashita & T. Watanabe (Tokyo: Universal Academy), 411
Larsson, J., Fransson, C., Alp, D., et al. 2019, ApJ, 886, 147
Larsson, J., Fransson, C., Sargent, B., et al. 2023, ApJL, 949, L27
Larsson, J., Fransson, C., Spyromilio, J., et al. 2016, ApJ, 833, 147
Lawrence, S. S., Sugerman, B. E., Bouchet, P., et al. 2000, ApJL, 537, L123
Lemen, J. R., Mewe, R., Schrijver, C. J., & Fludra, A. 1989, ApJ, 341, 474
Maggi, P., Haberl, F., Sturm, R., & Dewey, D. 2012, A&A, 548, L3
Maitra, C., Haberl, F., Sasaki, M., et al. 2022, A&A, 661, A30
Miceli, M., Orlando, S., Burrows, D. N., et al. 2019, NatAs, 3, 236
Ono, M., Nagataki, S., Ferrand, G., et al. 2020, ApJ, 888, 111
Orlando, S., Miceli, M., Petruk, O., et al. 2019, A&A, 622, A73
Orlando, S., Miceli, M., Pumo, M. L., & Bocchino, F. 2015, ApJ, 810, 168
Orlando, S., Ono, M., Nagataki, S., et al. 2020, A&A, 636, A22
Park, S., Zhekov, S. A., Burrows, D. N., et al. 2006, ApJ, 646, 1001
Park, S., Zhekov, S. A., Burrows, D. N., Garmire, G. P., & McCray, R. 2004, ApJ, 610, 275
Park, S., Zhekov, S. A., Burrows, D. N., & McCray, R. 2005, ApJL, 634, L73
Ravi, A. P., Park, S., Zhekov, S. A., et al. 2021, ApJ, 922, 140
Ravi, A. P., Park, S., Zhekov, S. A., et al. 2024, ApJ, 966, 147
Raymond, J. C., Ghavamian, P., Bohdan, A., et al. 2023, ApJ, 949, 50
Russell, S. C., & Dopita, M. A. 1992, ApJ, 384, 508
Singh, K. P., White, N. E., & Drake, S. A. 1996, ApJ, 456, 766
Sonneborn, G., Pun, C. S. J., Kimble, R. A., et al. 1998, ApJL, 492, L139
Sturm, R., Haberl, F., Aschenbach, B., & Hasinger, G. 2010, A&A, 515, A5
Sun, L., Orlando, S., Greco, E., et al. 2025, arXiv:2501.18091
Sun, L., Vink, J., Chen, Y., et al. 2021, ApJ, 916, 41
Vink, J. 2012, A&ARv, 20, 49
Vink, J. 2020, Physics and Evolution of Supernova Remnants (Cham: Springer)
West, R. M., Lauberts, A., Jorgensen, H. E., & Schuster, H. E. 1987, A&A, 177, L1
Wilms, J., Allen, A., & McCray, R. 2000, ApJ, 542, 914
Zhekov, S. A., McCray, R., Borkowski, K. J., Burrows, D. N., & Park, S. 2006, ApJ, 645, 293
Zhekov, S. A., McCray, R., Dewey, D., et al. 2009, ApJ, 692, 1190
Zhekov, S. A., Park, S., McCray, R., Racusin, J. L., & Burrows, D. N. 2010, MNRAS, 407, 1157